Antarctic ice-shelf advance driven by anomalous atmospheric and sea-ice circulation

Frazer D.W. Christie[1*], Toby J. Benham[1], Christine L. Batchelor[1,2], Wolfgang Rack[3], Aleksandr Montelli[1] and Julian A. Dowdeswell[1]

[1]Scott Polar Research Institute, University of Cambridge, Cambridge, CB2 1ER, UK

[2]Now at: School of Geography, Politics and Sociology, University of Newcastle, Newcastle, NE1 7RU, UK

[3]Gateway Antarctica, University of Canterbury, Private Bag 4800, Christchurch 8140, New Zealand

*Corresponding author: Frazer D. W. Christie, fc475@cam.ac.uk

Antarctic ice-shelf advance driven by anomalous atmospheric and sea-ice circulation

Frazer D.W. Christie[1*], Toby J. Benham[1], Christine L. Batchelor[1,2], Wolfgang Rack[3], Aleksandr Montelli[1] and Julian A. Dowdeswell[1]

[1]Scott Polar Research Institute, University of Cambridge, Cambridge, CB2 1ER, UK

[2]Now at: School of Geography, Politics and Sociology, University of Newcastle, Newcastle, NE1 7RU, UK

[3]Gateway Antarctica, University of Canterbury, Private Bag 4800, Christchurch 8140, New Zealand

*Corresponding author: Frazer D. W. Christie, fc475@cam.ac.uk

Abstract:

The disintegration of the eastern Antarctic Peninsula's Larsen A and B ice shelves has been attributed to atmosphere and ocean warming, and increased mass-losses from the glaciers once restrained by these ice shelves have increased Antarctica's total contribution to sea-level rise. Abrupt recessions in ice-shelf frontal position presaged the break-up of Larsen A and B, yet, in the ~20 years since these events, documented knowledge of frontal change along the entire ~1,400 km-long eastern Antarctic Peninsula is limited. Here, we show that 85% of the seaward ice-shelf perimeter fringing this coastline underwent uninterrupted advance between the early 2000s and 2019, in contrast to the two previous decades. We attribute this advance to enhanced ocean-wave dampening, ice-shelf buttressing and the absence of sea-surface slope-induced gravitational ice-shelf flow. These phenomena were, in turn, enabled by increased near-shore sea ice driven by a Weddell Sea-wide intensification of cyclonic surface winds around 2002. Collectively, our observations demonstrate that sea-ice change can either safeguard from, or set in motion, the final rifting and calving of even large Antarctic ice shelves.

Main Text:

Ice shelves fringe ~75% of the Antarctic Ice Sheet and inhibit unrestrained discharge of grounded ice to the ocean[1]. When in a state of mass equilibrium, these ice shelves flow towards the ocean from the 'grounding line' – the location where grounded ice first begins to float – at a rate proportional to inland ice-sheet accumulation, and spread, thin and fracture towards their seaward limits before calving. However, satellite observations[2-9] have revealed the climate change-related mass imbalance of many of Antarctica's coastal regions, which, in the Antarctic Peninsula, has culminated in the accelerated disintegration of several ice shelves[2-5,9] (Figure 1). Whereas the precise mechanisms driving ice-shelf disintegration and their links to long-term climate change remain elusive, the demise of the Larsen A (1995) and B (2002) ice shelves of the eastern Antarctic Peninsula (EAP) has been attributed largely to regional atmospheric warming instigating surface melt-induced hydrofracturing of the shelf ice[2-5,9-11]. Other ice-shelf weakening processes, including ocean-driven basal melting[12-13] and ice-flow acceleration[14], are also suggested to have augmented Larsen A and B's propensity for decay. Together, these phenomena led to the abrupt calving-induced recession of Larsen A and B's frontal positions prior to and during their disintegration[2-5,9] (Figure 1).

Having become an exemplar for the fate of the Antarctic Ice Sheet under a warming climate, frontal recession like that observed at Larsen A and B is considered to be a useful diagnostic for ice-sheet-shelf instability[5,15-16]. Since the early 2000s, however, few high-resolution measurements of frontal position exist along the ~1,400 km of shelf ice fringing the EAP[5,17], despite evidence of surface melting historically encroaching upon many of the ice shelves there[18]. Here, we use high-resolution satellite observations to show that most shelf ice fringing the EAP underwent sustained advance over the approximately two-decade period following Larsen B's collapse (*c.* 2003-2019), contrary to earlier episodes of marked frontal retreat between *c*. 1982 and 2002. We couple our observations with atmosphere and ocean reanalyses and long-term satellite records to link this advance to a regional, wind-driven stabilizing effect imparted on the ice shelves by increased concentrations of near-shore sea ice.

Ice-shelf and glacier change

Between one of the last complete surveys of the coastline in 2003/4[17] and 2019, our satellite-derived frontal observations (Methods; Supplementary Data 1) show that 85% of the EAP's seaward ice-shelf perimeter underwent uninterrupted advance (Figures 1 and 2; Supplementary Data 2). This includes the progressive, seaward expansion of Ronne Ice Shelf, whose margin is partially nourished by the EAP's southernmost glaciers. The only exceptions to this advance were at SCAR Inlet Ice Shelf, which until 2009 continued to retreat following the 2002 disintegration of Larsen B, and Larsen C Ice Shelf, which underwent a relatively small (1,300 km^2) calving in 2004 and then later calved the colossal (6,000 km^2) iceberg A-68 from its southern margin in 2017[19] (Figures 1 and 2; Supplementary Discussion 1; Supplementary Video 1). No other significant calving events occurred along the EAP between these times, although, since 2019, supplementary observations reveal the later calving of icebergs from the Larsen D (A-69, A-70 and A-71 in 2020) and Ronne (A-76 in 2021) ice shelves (Figure 1; Supplementary Discussions 1 and 2; Supplementary Videos 2-4). Collectively, our observations of uninterrupted advance along most of the EAP between 2003/4 and 2019 contrast with the period *c*. 1982-2002, when more frequent ice-shelf calving events occurred intermittently along the coastline[2-5,9] (Figures 1 and 2).

Ice-shelf advance may occur in response to dynamically unstable changes near the grounding line; such changes governed the ice-flow acceleration of SCAR Inlet Ice Shelf following the 2002 demise of Larsen B[20] and, since 2009, explain our observations of ice-shelf advance there (Figures 1 and 2). To assess the role ice dynamics may have played in the advance of the ice shelves south of SCAR Inlet since 2002, we examined changes in the location of the EAP's grounding line – a sensitive indicator for ice-dynamic imbalance[21] – between the mid-1990s and present using satellite radar-based observations (Methods). Between the mid-1990s and 2016/17, we do not detect any significant change in grounding line location (GLL), with negligible migration observed along most of the EAP coastline (Extended Data Figures 1 and 2). Extending these records to 2019 at Larsen C Ice Shelf (Methods; Extended Data Figure 1), we also find no evidence for any recent GLL retreat, despite the calving of iceberg A-68 in 2017 (Figure 1). Alongside observations of negligible post-calving acceleration in grounded ice flow as constrained from recent satellite-derived ice velocity products (Methods; Extended Data Figure 3), these findings suggest that A-68's calving did not induce an ice-dynamic response landward of Larsen C between 2017 and 2019. Such behaviour is consistent with earlier modelling efforts predicting the glaciological implications of A68's calving[1], and with trends of constant or slightly decreased ice mass losses along most of the EAP throughout the satellite era[21,22] (Extended Data Figure 3). Overall, our observations demonstrate a dearth of dynamic-induced change near the EAP's grounding line south of SCAR Inlet since at least the mid-1990s. Low rates of ice-shelf basal melting since 1992[13,23] support this finding, and further imply that the observed, ~20-year advance of the EAP's ice shelves south of SCAR Inlet is not related to variable ocean forcing.

Atmospheric processes and sea-ice circulation

In the absence of ice-dynamical change at the grounding line, the advance of the EAP coastline between 2003/4 and 2019 may have been related to a change towards more positive surface mass-balance conditions over the ice shelves themselves. To test for this, we examined the historical climatology of the region using ECMWF ERA5 global atmospheric reanalysis outputs (Methods). Consistent with earlier research[23-24], we detect an anomalous, Antarctic Peninsula-wide reduction in mean austral summertime near-surface temperature between 2003 and 2019 (Supplementary Figure 1). This implies that the amount of surface melting on these ice shelves decreased and did not propagate south during this timeframe relative to all earlier summers on record (1979-2002), including the period *c.* 1982-2002 when we detect more frequent iceberg calving events along the EAP coast (Figure 2). By implication, therefore, the susceptibility for ice-shelf calving related to meltwater-induced thinning, weakening and hydrofracture will have lessened. This interpretation is supported by long-term satellite observations at Larsen C[25] and, alongside an observed thickening of this ice shelf in recent years[23,26], may have contributed to its advance before and after the calving of iceberg A-68 in 2017 (Figures 1 and 2). Poleward of Larsen C, however, we expect that this phenomenon played a negligible role in the stability of the EAP's ice shelves, given the much colder summertime surface temperatures (and hence reduced volumes of surface melt) found towards the interior of the continent. Beyond surface melting, minimal change in annual-averaged precipitation rates south of SCAR Inlet (Supplementary Figure 1) are also unlikely to have reinforced the ice shelves significantly, and so cannot explain their ~20-year advance.

Offshore from the EAP, however, we detect a contemporaneous reduction in summertime temperature which enveloped the entire Weddell Sea between 2003 and 2019 (Supplementary Figure 1). This reduction, linked to an array of climatic forcing mechanisms (Supplementary Discussion 3; Extended Data Figure 4), coincided with a pronounced intensification of cyclonic near-surface winds relative to all earlier times on record (Figure 3) and a related, pervasive increase in both summertime and annual-averaged sea-ice cover (Figure 3; Extended Data Figure 5). Alongside a year-round suppression of seaward-blowing winds over the ice sheet (Extended Data Figure 4), this intensified cyclonic circulation enhanced both the delivery of pack ice towards the EAP (Figure 3) and the consolidation of landfast sea ice immediately offshore of most ice shelves (Extended Data Figure 6; Supplementary Discussions 1 and 3). Compared with the period *c.* 1982-2002 in particular, these observations are confirmed by clear increases in summertime- (Figure 2) and annual-averaged (not shown) sea-ice concentration (SIC) anomalies offshore of each ice shelf. Indeed, between 2003 and 2019, EAP mean summertime SIC anomalies were 5% higher on average relative to *c*. 1982-2002 (Figure 2; Extended Data Figure 5), and no values fell below the extreme (2-3σ) sea-ice minimum anomalies observed during this earlier period.

Sea ice-enabled fortification of ice shelves

Given the lack of ice-dynamic and surface mass-balance change south of SCAR Inlet since *c.* 2000 (Figure 3; Extended Data Figures 1-3; Supplementary Figure 1), our observations imply that an alternative forcing mechanism facilitated the ~20-year advance of the ice shelves located there. The variable geometries yet generally synchronous historical behaviour (*c*. 1982-2002) of these ice shelves further implicates the role of such forcing, because ice shelves of different sizes, thicknesses and ice-flow velocities would otherwise be expected to exhibit disparate calving periodicities if internal glaciological stresses governed the final rifting and calving of icebergs alone. We therefore suggest that the two-decade advance of the EAP can be explained by the anomalous Weddell Sea-wide increase in SIC we observe since 2002. The sea-ice-related processes contributing to this advance are summarised in Figure 4, and are discussed further below.

Recent work has correlated the timing of the Larsen A and B ice shelves' disintegration to heightened ice-shelf flexure and fatigue brought about by the effects of damaging ocean waves[27]. At these locations, waves were of sufficient (10-20 s period) energy to trigger strain-induced rifting and calving of the ice front, which in turn initiated catastrophic ice-shelf collapse. The transmission of such waves to the front of both ice shelves was enabled by significant sea-ice free ocean conditions in the summertime months preceding collapse, which permitted the direct migration of far-sourced swell waves across the typically sea-ice covered Weddell Sea[27]. Under 'normal' sea-ice conditions, which in the western Weddell Sea represent ~80-100% year-round pack ice cover ≥2 m thick[28-29], modelling experiments[27] suggest that this damaging wave energy would have instead been dissipated by ~65% only 0.1-20 km into pack ice. These findings alone therefore imply that the anomalous post-2002 increase in Weddell Sea-wide SIC we observe (Figure 3; Extended Data Figures 5 and 6) functioned to bolster the defence of the EAP from the ocean, thereby minimising the potential for wave-induced ice-shelf damage.

Prior to 2003, analyses of the SIC record in conjunction with ERA5 ocean wave reanalysis data (Methods) further demonstrate the importance of sea ice in governing the stability of the EAP's ice shelves. That is, analogous to the ocean conditions preceding the demise of Larsen A and B[27], we identify four 'open ocean years' in which exceptional summertime sea-ice losses were of sufficient magnitude and extent to enable wave-based damage of two or more ice shelves along the coast (Extended Data Figure 7). These years are indicated in Figure 2 and, with reference to recent modelling experiments investigating the influence of ocean waves on ice-shelf integrity[27,30], represent times when incoming waves would have been of significant height and period to increase ice-frontal strain by up to five-to-seven orders of magnitude ($\mathcal{E}$ = ~10^{-12} to 10^{-7}-10^{-5}) depending on ice-shelf thickness (Supplementary Discussion 4). Alongside background rift propagation by internal glaciological stresses, we expect that these events were of sufficient force to augment the weakening of all but one of the EAP's exposed ice shelves between *c*. 1982 and 2002, in contrast to the dampened, increasingly sea-ice covered conditions after this time (Figures 2 and 3; Extended Data Figure 5). The exception to this phenomenon is Ronne Ice Shelf, whose thickness (>250 m) renders its front immune to wave-based damage (Supplementary Discussion 4). Notwithstanding Ronne Ice Shelf, of the 'open ocean years' we observe offshore of all other ice shelves (Figure 2), 80% were followed by large-scale calving events within two years. These near-concurrent events constitute half of all EAP calving events on record.

It is important to note, however, that the modelling experiments discussed above predict the zone of maximum wave-induced strain on an ice shelf to reside only several kilometres from the ice front[27]. Although such strain may have weakened the seaward extremities of these ice shelves and can explain, for example, the small 'sliver-type' calving of the Larsen A and B ice shelves prior to their collapse[3,9,27], swell waves could not therefore have triggered the larger calving events observed along the EAP coastline alone (Figure 2). Apart from a one-off, high-energy tsunami wave (>20 s period) which instigated the 2004 calving of Larsen C Ice Shelf[31] (Figure 2; Supplementary Discussion 4), we identify two interrelated processes that governed these events.

First, we suggest that (near-)contemporaneous ice-shelf debuttressing played a key role in inducing the final rifting and calving of most of the EAP's exposed ice shelves (cf. Supplementary Discussion 2). Recent observations of Larsen D Ice Shelf's 2020 ice-frontal behaviour offer compelling evidence for the effects of such debuttressing, when strong offshore winds of comparable magnitude and direction to those observed across the EAP *c*. 1980-2002 (Extended Data Figure 4, Supplementary Discussion 3) drove the rapid evacuation of dense, highly pressurised pack ice from the coast immediately prior to the calving of icebergs A-69, A-70 and A-71 (Figure 1; Supplementary Videos 2 and 3). In a region normally covered by year-round, 100% sea-ice cover[29], this phenomenon instigated near-instantaneous increases in extensional strain upstream of Larsen D's ice front, triggering the breakaway of all three icebergs. In addition to the effects of rapid pack-ice evacuation, over longer (seasonal-to-decadal) timescales, satellite observations show that localised reductions in landfast sea ice fringing the coast will have played a further role in debuttressing the EAP, including at the Larsen C and D ice shelves (Extended Data Figure 6; Supplementary Discussion 1). At Larsen C in particular, we suggest that such reductions near its heavily crevassed southernmost front had especial importance for the calving of iceberg A-68 in 2017 (Figure 1; Supplementary Video 1).

Secondly, and in unison with the effects of sea-ice debuttressing, concurrent HYCOM-derived sea-surface height records (Methods) reveal the presence of anomalously steep, oceanward slopes in the formerly sea-ice sheltered waters bordering Larsen D prior to its 2020 calving events (Extended Data Figure 8). Driven by the same offshore winds controlling the rapid evacuation of sea-ice discussed above, this phenomenon acted to maximise ice-shelf frontal strain (and hence rifting) by means of enhanced gravitational flow towards the ocean. Similar wind- and sea-ice loss-enabled ocean sloping has recently been implicated as the trigger mechanism behind the calving of iceberg D-28 from Amery Ice Shelf in 2019[32], suggesting that pronounced sea-surface slopes can instigate the final weakening and breakaway of large icebergs from even very thick (and swell-wave immune) ice shelves. Notably, we show that similar phenomena heralded the 2002 collapse of Larsen B Ice Shelf, presaged the breakaway of giant iceberg A-76 from Ronne Ice Shelf in 2021 (Supplementary Discussion 2; Supplementary Video 4); and therefore likely contributed to the calving of, for example, colossal icebergs A-20 and A-38 from the Larsen C and Ronne ice shelves in 1986 and 1998, respectively (Figures 1 and 2; Extended Data Figure 8; Supplementary Discussion 2). A dearth of long-term, high-repeat-pass satellite and sea-surface height records prior to 2000, however, precludes any further detailed insight into historical sea ice, ocean, and ice-shelf change.

In contrast to the 'open ocean years' described above, we note that the recent calving events at Larsen D (A-69, A-70, A-71) and Ronne (A-76) were, however, not preconditioned by region-wide sea-ice loss and potentially damaging ocean waves, revealing that rapid, coastal-only sea-ice evacuation and associated (and generally shallower and less energetic; compare Extended Data Figure 8b with 8d, 8f and 8h) sea-surface slope changes can be sufficient to trigger calving. We detect three earlier times in which analogous, pervasive offshore wind-driven sea-ice evacuation (>2σ SIC loss) occurred within a temporal window associated with a 'non-open ocean year' EAP calving event (Figure 2; Extended Data Figures 9 and 10). As for Larsen D

Ice Shelf in 2020, these concurrent sea-ice evacuation and calving events only occurred when the ice shelves were at or near their most seaward positions since records began (Figures 1 and 2), when their fronts would have been thinnest and most susceptible to breakoff due to accumulated internal strain. Given that other periods of wind-driven sea-ice evacuation have occurred intermittently throughout the climatological record (not shown), these findings suggest that, when acting alone, coastal sea-ice evacuation only serves as a calving trigger for the most structurally vulnerable ice shelves.

Future sea ice—ice shelf interactions

Our observations present strong evidence for the importance of sea ice in modulating the stability of Antarctica's coastal margin. Specifically, we show that the ~20-year advance of the EAP's ice shelves can be linked to heightened fortification against potentially damaging ocean waves, increased ice-shelf buttressing and/or the related absence of sea-surface slope-induced gravitational flow, all of which were afforded by regional-scale sea-ice increases since *c*. 2002. Indeed, in almost all (94%) cases throughout the satellite era, EAP calving only occurred during or shortly after the removal of sea ice in some form, demonstrating that abrupt changes in sea-ice cover can safeguard from, or set in motion, the final weakening and calving of even large ice shelves.

Whereas significant reductions in Weddell Sea sea-ice cover are not expected imminently[33], current climate model simulations predict wholescale circum-Antarctic sea-ice losses by 2100 under a range of emissions scenarios[33]. Prevalent across all seasons[33], these simulations suggest that any current or near-future stabilising effects associated with increased sea-ice cover may only be short-lived. Future increases in ocean-driven basal melting of Antarctica's ice shelves[34-35] may confound these effects by expediting the erosion of shelf ice to the point of calving. Conversely, other studies have suggested that enhanced basal melting may contribute to the future, temporary expansion of sea-ice cover around Antarctica, through the accumulation of cold, low-salinity meltwater in the upper layers of the Southern Ocean[36-37]. Critically, this phenomenon is not accounted for in the climate models detailed above, and implies that – like the processes that we show are currently at work in the EAP – increased future sea-ice cover may instead act to temporarily offset net ice-sheet mass losses by impeding the calving-related deterioration of Antarctica's ice shelves. Regardless of how circum-Antarctic sea ice changes in a warming climate, our observations highlight the complexity and often-overlooked importance of sea-ice variability to the health of the Antarctic Ice Sheet.

Acknowledgments: We thank A. Cook, T. Haran, J. Ferrigno and J. Wuite for making their historical ice-shelf frontal positions publicly available, D. Floricioiu for providing access to the DLR/ESA AIS CCI GLL product and NASA, USGS, ESA, the EU Copernicus programme, NSIDC, ECWMF, NOAA, G. Marshall and A. Fraser for making all other satellite and climate data utilised in this study available free of charge. This work was funded by the Flotilla Foundation and Marine Archaeology Consultants Switzerland (to FDWC, TJB, CLB, AM, and JAD) and with the financial assistance (to FDWC and JAD) of the Prince Albert II of Monaco Foundation.

Author Contributions: FDWC devised the study and carried out all acquisition, processing and interpretation of the observational and climate reanalysis datasets referred to in the text. TJB, WR, CLB and AM assisted FDWC with the initial acquisition and processing of the Sentinel-1A/B data. FDWC wrote the manuscript, and each co-author contributed comments on the text and figures.

Competing Interests: The authors declare no competing interests.

Main Text Figures and Captions:

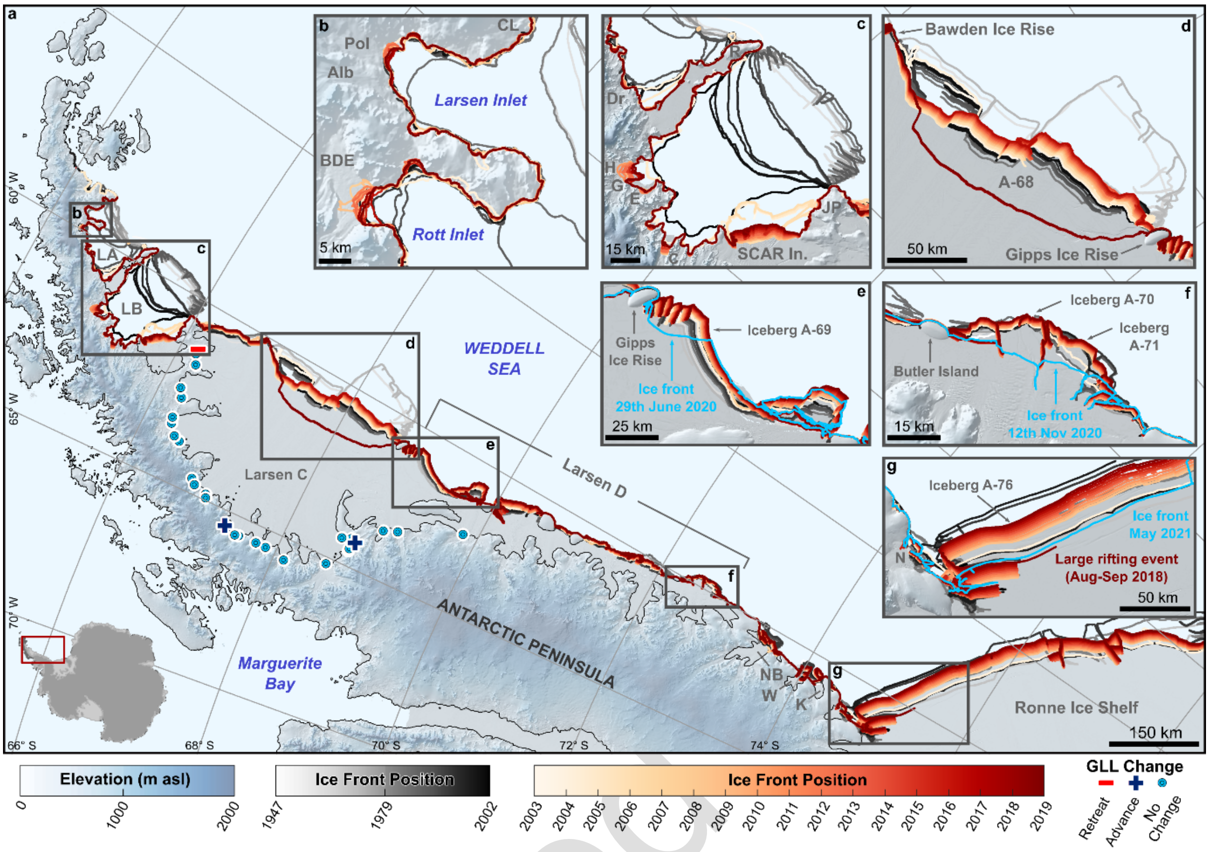

Figure 1 | Ice-shelf front and grounding-line migration in the eastern Antarctic Peninsula south of Cape Longing. ***a***, Ice-shelf frontal positions spanning each of the EAP's major ice shelves (SCAR Inlet, Larsen C, Larsen D, New Bedford (*NB*), Wright (*W*), Keller (*K*) and Ronne; see Methods for data sources), including the former extent of Larsen A (*LA*) and B (*LB*) and their modern-day coastlines. Over the grounding zone of Larsen C Ice Shelf, symbols indicating recent (2016/7-2019) grounding-line migration are also shown (see main text, Methods and Extended Data Figures 1 and 2 for further information). ***b-g***, detail. *Pol* denotes Polaris; *Alb*, Albone; *BDE*, Bombardier-Dinsmoor-Edgeworth; *Dr*, Drygalski; *H*, Hektoria; *G*, Green; *E*, Evans and *C*, Crane glaciers; *CL*, Cape Longing; *R*, Robertson Island; *JP*, Jason Peninsula, *A-68*, iceberg A-68 and *N*, Nantucket Inlet.

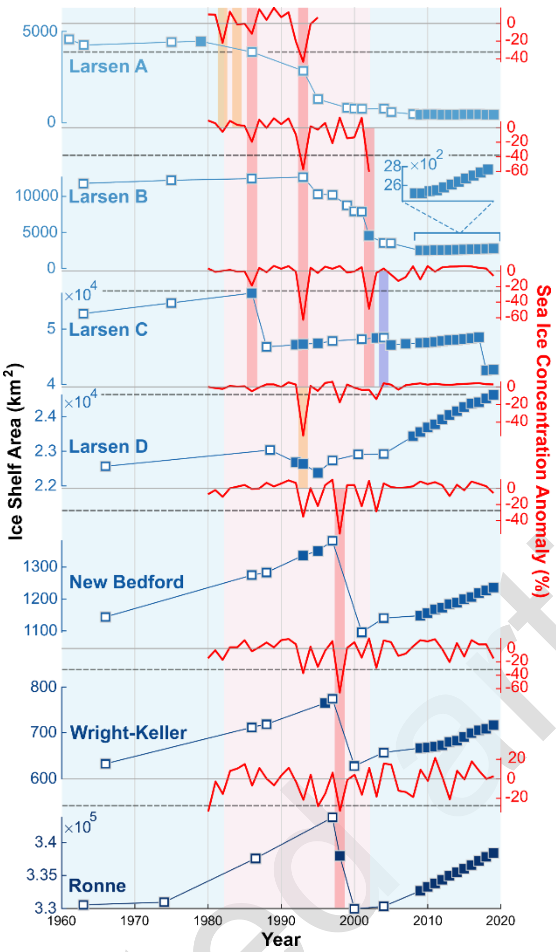

Figure 2 | Areal evolution of the EAP's ice shelves, 1961-2019. Blue lines denote linear trend between successive observations (squares) to emphasise net change in area between these times; solid squares, new observations presented in this study. For simplicity, the confluent Wright and Keller ice shelves are presented as a single entity. Also shown are mean summertime sea-ice concentration (SIC) anomalies offshore of each ice shelf for the period 1979-2019 (red; see Extended Figure 5 for averaging regions). Dashed horizontal lines denote 2σ below SIC mean. Blue (pink) shading denotes the timing of relatively cool (warm) climatic conditions conducive to pervasive coastal sea-ice increase (decrease) (cf. Supplementary Discussion 3). Dark pink shading denotes ice-shelf 'open ocean years'; yellow, coastal-only sea-ice evacuation events; dark blue, timing of a tsunami event linked to the 2004 calving of Larsen C Ice Shelf (cf. main text, Supplementary Discussion 4 and Extended Data Figures 7-10).

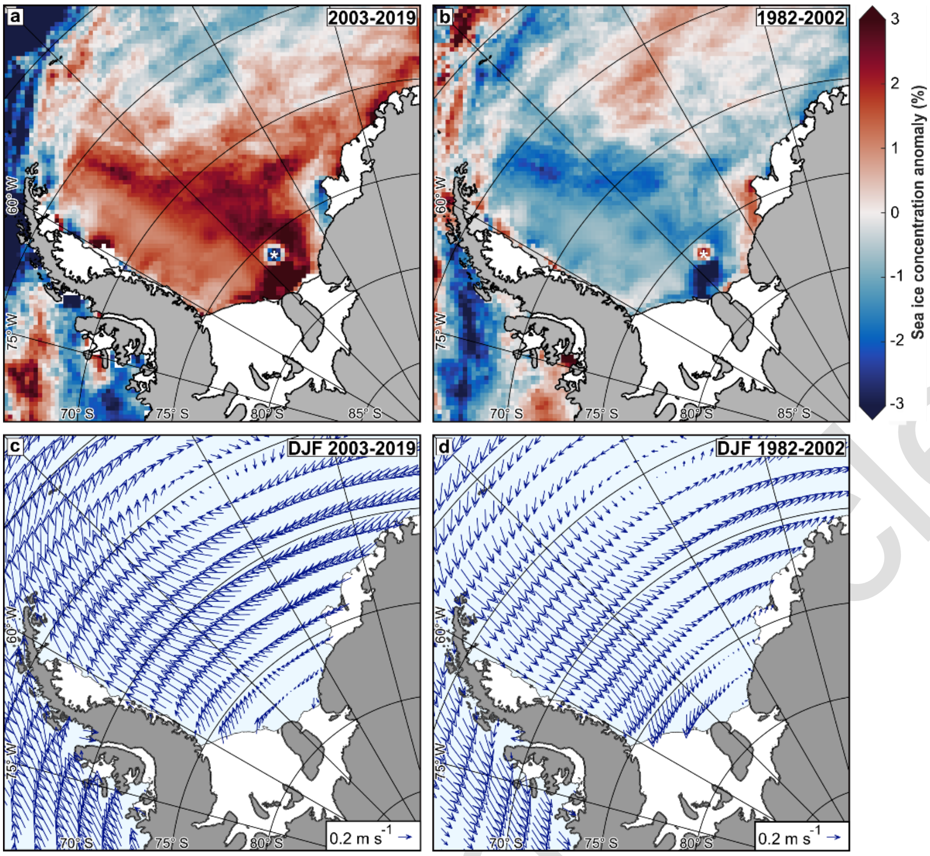

Figure 3 | Sea-ice concentration and surface-wind conditions over the Weddell Sea Sector. ***a***, Mean passive microwave-derived sea-ice concentration anomalies for all months between January 2003 and December 2019 (inclusive), relative to all months on record (1979-2019). White asterisk denotes the approximate location of iceberg A-23a (lightly grounded at this location since 2000); light grey shading, no data. ***b***, Same as ***a***, but for all months between January 1982 and December 2002 (following Figure 2 and Extended Data Figure 4). ***c*** and ***d***, Mean ERA5-derived 10 m wind direction and magnitude anomalies (vectors) for all complete austral summertime (DJF) cycles between 2003 and 2019 and 1982 and 2002, respectively, relative to all complete summertime cycles on record (1980-2019). Relative to the cyclonic (clockwise) flow of the Weddell Gyre, the reversal in anomalous wind direction observed in *d* denotes diminished cyclonic flow (i.e. towards more anti-cyclonic conditions).

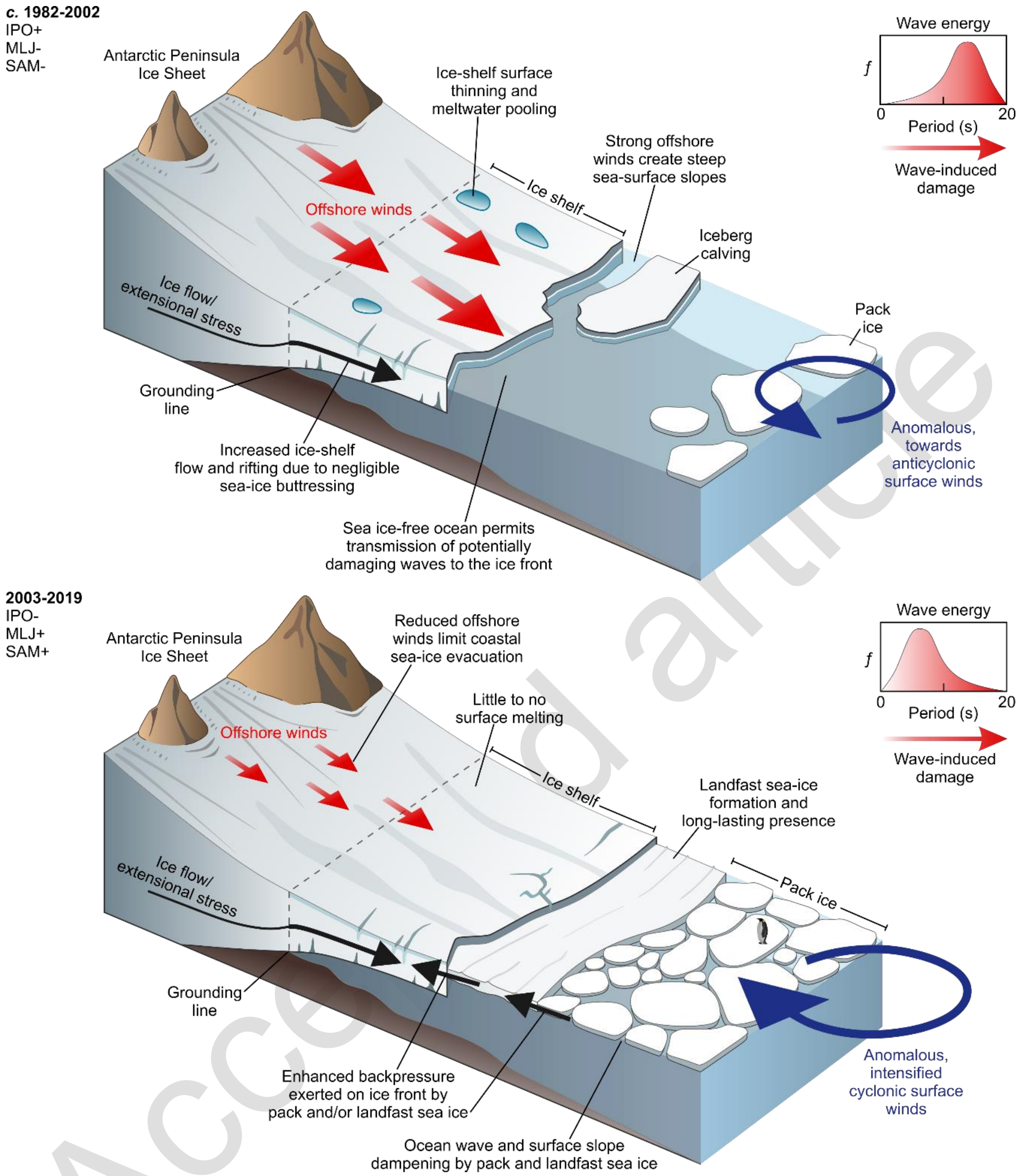

Figure 4 | Schematic diagrams showing the key atmospheric and sea ice processes controlling the (in)stability of the EAP's ice shelves through time. The signs following IPO, MJL and SAM refer to the state of the Interdecadal Pacific Oscillation, Mid-Latitude Jet and Southern Annular Mode relative to each epoch, respectively (Supplementary Discussion 3). Histograms indicate probability of ocean wave-induced ice-shelf frontal damage. Note that, unlike the EAP's other ice shelves, Ronne Ice Shelf is immune to the influence of damaging ocean waves given its thickness (Supplementary Discussion 4).

References

(1) Fürst, J. J., Durand, G., Gillet-Chaulet, F., Tavard, L., Rankl, M., Braun, M. & Gagliardini, O. The safety band of Antarctic ice shelves. *Nat. Clim. Change* **6(5)**, 479–482 (2016). doi: 10.1038/nclimate2912.

(2) Rott, H., Skvarca, P. & Nagler, T. Rapid collapse of Northern Larsen Ice shelf, Antarctica. *Science* **271(5250)**, 788–792 (1996). doi:10.1126/science.271.5250.788.

(3) Scambos, T. A., Hulbe, C., Fahnestock, M. & Bohlander, J. The link between climate warming and break-up of ice shelves in the Antarctic Peninsula. *J. Glaciol.* **46(154)**, 516–530 (2000). doi:10.3189/172756500781833043.

(4) Scambos, T., Hulbe, C. & Fahnestock, M. Climate-induced ice shelf disintegration in the Antarctic peninsula. In (Domack E., Leventer, A., Burnet, A., Bindschadler, R., Convey, P., & Kirby, M. (eds.)), *Antarctic Peninsula Climate Variability: Historical and Paleoenvironmental Perspectives*, **79**, 79–92 (2003). doi:10.1029/AR079p0079.

(5) Cook, A. J. & Vaughan, D. G. Overview of areal changes of the ice shelves on the Antarctic Peninsula over the past 50 years. *Cryosphere* **4**, 77–98 (2010). doi:10.5194/tc-4-77-2010.

(6) The IMBIE team. Mass balance of the Antarctic Ice Sheet from 1992 to 2017. *Nature* **558**, 219–222 (2018). doi:10.1038/s41586-018-0179-y.

(7) Shepherd, A. *et al*. Trends in Antarctic Ice Sheet Elevation and Mass. *Geophys. Res. Lett.* **46(14)**, 8174–8183 (2019). doi: 0.1029/2019GL082182.

(8) Paolo, F. S., Fricker, H. A. & Padman, L. Volume loss from Antarctic ice shelves is accelerating. *Science* **348(6232)**, 327–331 (2015). doi:10.1126/science.aaa0940.

(9) Rack, W. & Rott, H. Pattern of retreat and disintegration of the Larsen B ice shelf, Antarctic Peninsula. *Ann. Glaciol.* **39**, 505–510 (2004). doi:10.3189/172756404781814005.

(10) van den Broeke, M. Strong surface melting preceded collapse of Antarctic Peninsula ice shelf. *Geophys. Res. Lett.* **32(12)**, L12815 (2005). doi:10.1029/2005GL023247.

(11) Banwell, A., MacAyeal., D. R. & Sergienko, O. V. Breakup of the Larsen B Ice Shelf triggered by chain reaction drainage of supraglacial lakes. *Geophys. Res. Lett.* **40(22)**, 5872–5876 (2013). doi:10.1002/2013GL057694.

(12) Etourneau, J. *et al*. Ocean temperature impact on ice shelf extent in the eastern Antarctic Peninsula. *Nat. Commun.* **10(1)**, 8–15 (2019). doi:10.1038/s41467-018-08195-6.

(13) Shepherd, A., Wingham, D., Payne, T. & Skvarca, P. Larsen Ice Shelf Has Progressively Thinned. *Science* **302**, 856–860 (2004). doi:10.1126/science.1089768.

(14) Rignot, E., Casassa, G., Gogineni, P., Krabill, W., Rivera, A. & Thomas, R. Accelerated ice discharge from the Antarctic Peninsula following the collapse of Larsen B ice shelf, *Geophys. Res. Lett.* **31**, L18401 (2004). doi:10.1029/2004GL020697.

(15) Miles, B. W. J., Stokes, C. R. & Jamieson, S. S. R. Simultaneous disintegration of outlet glaciers in Porpoise Bay (Wilkes Land), East Antarctica, driven by sea ice break-up. *Cryosphere* **11**, 427–442 (2017). doi:10.5194/tc-11-427-2017.

(16) MacGregor, J. A., Catania, G. A., Markowski, M. I. S. & Andrews, A. G. Widespread rifting and retreat of ice-shelf margins in the eastern Amundsen Sea Embayment between 1972 and 2011. *J. Glaciol.* **58(209)**, 458–466 (2012). doi:10.3189/2012JoG11J262.

(17) Haran, T., Bohlander, J., Scambos, T., Painter, T. & Fahnestock, M. MODIS Mosaic of Antarctica 2003-2004 (MOA2004) Image Map, Version 1. Boulder, Colorado USA. NASA National Snow and Ice Data Center Distributed Active Archive Center (2005, updated 2019). doi:10.7265/N5ZK5DM5.

(18) Bell, R. W., Banwell, A. F., Trusel, L. D. & Kingslake, J. Antarctic surface hydrology and impacts on ice-sheet mass balance. *Nat. Clim. Change* **8(12)**, 1044–1052 (2018). doi:10.1038/s41558-018-0326-3.

(19) Hogg, A. E. & Gudmundsson, H. Impacts of the Larsen-C Ice Shelf calving event, *Nat. Clim. Change* **7(8)**, 540–542 (2017). doi:10.1038/nclimate3359.

(20) Wuite, J. *et al*. Evolution of surface velocities and ice discharge of Larsen B outlet glaciers from 1995 to 2013. *Cryosphere* **9(3)**, 957–969 (2015). doi:10.5194/tc-9-957-2015.

(21) Rignot, E. *et al*. Four decades of Antarctic Ice Sheet mass balance from 1979–2017. *Proc. Natl. Acad. Sci. U.S.A.* **116(4)**, 1095–1103 (2019). doi:10.1073/pnas.1812883116.

(22) Velicogna, I. *et al*. Continuity of Ice Sheet Mass Loss in Greenland and Antarctica From the GRACE and GRACE Follow-On Missions. *Geophys. Res. Lett.* **47**, e2020GL087291 (2020). doi:10.1029/2020GL087291.

(23) Adusumilli, S., Fricker, H. A., Siegfried, M. R., Paolo, F. S. & Ligtenberg, S. R. M. Variable Basal Melt Rates of Antarctic Peninsula Ice Shelves, 1994–2016. *Geophys. Res. Lett.* **45(9)**, 4086–4095 (2018). doi: 10.1002/2017GL076652.

(24) Turner, J. *et al*. Absence of 21st century warming on Antarctic Peninsula consistent with natural variability. *Nature* **535**, 411–415 (2016). doi:10.1038/nature18645.

(25) Bevan, S. L. *et al*. Decline in Surface Melt Duration on Larsen C Ice Shelf Revealed by The Advanced Scatterometer (ASCAT). *Earth Space Sci.* **5(10)**, 578–591 (2018). doi: 10.1029/2018EA000421.

(26) Smith, B. *et al*. Pervasive ice sheet mass loss reflects competing ocean and atmosphere processes. *Science* **368(6496)**, 1239–1242 (2020). Doi: 10.1126/science.aaz5845.

(27) Massom, R. A. *et al*. Antarctic ice shelf disintegration triggered by sea ice loss and ocean swell. *Nature* **558**, 383–389 (2018). doi:10.1038/s41586-018-0212-1.

(28) Kacimi, S. & Kwok, R. The Antarctic sea ice cover from ICESat-2 and CryoSat-2: freeboard, snow depth, and ice thickness. *Cryosphere* **14**, 4453–4474 (2020). doi:10.5194/tc-14-4453-2020.

(29) Dowdeswell, J. A., et al. Sea-floor and sea-ice conditions in the western Weddell Sea, Antarctica, around the wreck of Sir Ernest Shackleton's *Endurance*. *Ant. Sci.* **32(4)**, 301–313 (2020). doi:10.1017/S0954102020000103.

(30) Sergienko, O. V. Elastic response of floating glacier ice to impact of long-period ocean waves. *J. Geophys. Res.* **115**, F04028 (2010). doi:10.1029/2010JF001721.

(31) Walker, C. C., Basis, J. N., Fricker, H. A., & Czerwinski, R. J. Structural and environmental controls on Antarctic ice shelf rift propagation inferred from satellite monitoring. *J. Geophys. Res. Earth Surface* **118**, 2354–2364 (2013). doi: 10.1002/2013JF002742.

(32) Francis, D., *et al.* Atmospheric extremes caused high oceanward sea surface slope triggering the biggest calving event in more than 50 years at the Amery Ice Shelf. *Cryosphere* **15**, 2147-2165 (2021). doi: 10.5194/tc-15-2147-2021.

(33) Intergovernmental Panel on Climate Change (IPCC). Polar Regions. In *The Ocean and Cryosphere in a Changing Climate: Special Report of the Intergovernmental Panel on Climate Change*, Cambridge: Cambridge University Press, pp. 203–320, doi:10.1017/9781009157964.005 (2022).

(34) Holland, P. R., Bracegridle, T. J., Dutrieux, P., Jenkins, A. & Steig, E. J. West Antarctic ice loss influenced by internal climate variability and anthropogenic forcing, *Nat. Geosci.* **12**, 718–724 (2019). doi:10.1038/s41561-019-0420-9.

(35) Naughten, K. A. *et al*. Future Projections of Antarctic Ice Shelf Melting Based on CMIP5 Scenarios. *J. Clim.* **31(13)**, 5243–5261 (2018). doi:10.1175/JCLI-D-17-0854.1.

(36) Bintanja, R., van Oldenborgh, G. J., Drijfhout, S. S., Wouters, B. & Katsman, C. A. Important role for ocean warming and increased ice-shelf melt in Antarctic sea-ice expansion. *Nat. Geosci.* **6(5)**, 376–379 (2013). doi:10.1038/ngeo1767.

(37) Bintanja, R., Oldenborgh, G. J. v., & Katsman, C. A. The effect of increased fresh water from Antarctic ice shelves on future trends in Antarctic sea ice, *Ann. Glaciol.* **56(59)**, 120–126 (2015). doi:10.3189/2015AoG69A001.

Methods

Ice-shelf frontal positions

Historical ice-shelf frontal positions (1947-2008; Figure 1) were obtained from several previously published data sources, and include fronts derived from a range of aerial and spaceborne optical and synthetic aperture radar (SAR) imagery[5,20,38-39]. To augment these historical records, we derived annual ice-shelf frontal positions over the period 2009-2019 using NASA/USGS Landsat 7 (2009-2013), Landsat 8 (2013-2014) and Copernicus/European Space Agency (ESA) Sentinel-1A/B (2015-2019) imagery (Supplementary Data 1) acquired during austral summertime of each year (December, January, February). Austral summertime images were chosen to ensure adequate solar illumination of the Antarctic Peninsula by Landsat 7 and 8, and for temporal consistency with the historical surveys detailed above. Select non-summertime Sentinel-1A/B images (Supplementary Data 1) were also utilised to survey the recent the calving of icebergs A-69, A-70 and A-71 from Larsen D Ice Shelf in 2020 (Figure 1; Supplementary Discussion 1; Supplementary Videos 2 and 3) and A-76 from Ronne Ice Shelf in 2021 (Figure 1; Supplementary Discussion 2; Supplementary Video 4).

Landsat 7 and 8 imagery containing <20% cloud cover were acquired from the United States Geological Survey's 'Earth Explorer' data repository (https://earthexplorer.usgs.gov/) as Collection 1 Level-1GT (Systematic Terrain Correction) products, and we used the 15 m resolution panchromatic band (B08) in our analyses. Sentinel-1A/B imagery was acquired from ESA via the Alaskan Satellite Facility (ASF; https://search.asf.alaska.edu/#/) in Level-1 Ground Range Detected (GRD) Interferometric Wide (IW) Swath format (10 m spatial resolution; Supplementary Data 1). Prior to analysis, we removed additive thermal noise contaminating each GRD-IW image, and radiometrically calibrated each scene. All images were subsequently terrain corrected and orthorectified using the Reference Elevation Model of Antarctica (REMA)[40]. Prior to Sentinel-1A IW acquisition over the Antarctic Peninsula

(<2016), or where no routine Sentinel-1A/B GRD-IW coverage exists (e.g. over the southern limits of Ronne Ice Shelf), Sentinel-1A/B Extra Wide Swath (EW) GRD imagery was utilised. GRD-EW scenes were acquired and processed in the same way as for GRD-IW imagery, and have a spatial resolution of 40 m. Cloud-free, multispectral Sentinel-2A/B imagery was also used to supplement our Sentinel-1A/B-based analyses across regions of complex fast-flowing ice or mountainous terrain, where the side-looking imaging capabilities of Sentinel-1A/B made ice-frontal positions difficult to identify. Level-1C Top-of-Atmosphere reflectance Sentinel-2A/B images (Supplementary Data 1) were acquired free of charge from the Copernicus Open Access Sentinel Hub (https://scihub.copernicus.eu/dhus/#/home), and have a spatial resolution of 10 m.

Prior to 2009-2019, we also derived select ice frontal positions during the early-to-mid 1990s south of Larsen B Ice Shelf using ERS-1/2 SAR observations. These observations were not included in the generation of the historical timeseries datasets outlined above[5,20,38-39], and provide important additional insight into ice-shelf frontal behaviour during the otherwise relatively data sparse 1990s (Figure 2). Similar to our Sentinel-1 observations, we used ERS-1/2 Level-1 SAR Precision (12.5 m resolution) and Medium Resolution (75 m resolution) Image Products (L1 SAR IMP and SAR IMM) in our analyses (Supplementary Data 1), and derived ice frontal positions for the years 1992 (Larsen C, Larsen D), 1993 (Larsen C, Larsen D, New Bedford), 1995 (Larsen C, Larsen D, New Bedford) and 1996 (Wright and Keller). These data were acquired from the ESA Earth Observation Catalogue (https://eocat.esa.int/sec/#data-services-area). To shed light on the precise timing of Larsen C's small (1300 km^2) calving event *c*. 2004 (Figure 2), additional Landsat 7 imagery was also used to determine this ice shelf's frontal position over the period 2000-2008 (Supplementary Data 1).

All ice-frontal positions mapped in this study were delineated manually using standard GIS software. To calculate temporal change in ice-shelf areal extent (Figure 2; Supplementary Data 2), all ice-shelf frontal positions were bounded to the position of the grounding line compiled by Depoorter et al. (ref. 41). The lateral limits of Larsen A-D match those defined by Cook et al. (ref. 5). Historical ice-shelf areal extent was only calculated for years with complete ice-shelf frontal coverage, rather than interpolating data gaps for years with incomplete coverage.

To further supplement our ice-shelf areal change analyses at Larsen C Ice Shelf, where no high-resolution observations exist documenting the precise timing of the large calving event(s) between 1975 and 1988 (Figures 1 and 2), we also examined historical iceberg-tracking records covering the Weddell Sea region[42]. These records were obtained from the NASA Scatterometer Climate Record Pathfinder data archive (https://www.scp.byu.edu/data/iceberg/), and consist of satellite-derived iceberg positions from 1978 to present as observed by Brigham Young University (BYU) and the U.S. National Ice Center (USNIC). Analyses of these records revealed the precise timing of Larsen C Ice Shelf's calving event to be 1986, when icebergs A-20 (7,285 km^2) and A-21 (~ 2,400 km^2) detached from the coastline in close succession. Using this information, Larsen C's 1986 areal extent (Figure 2) was ascertained from the linear fit of all earlier, higher resolution measurements.

Similar to the iceberg-tracking records detailed above, we also deduced Ronne Ice Shelf's 1998 areal extent (Figure 2; Supplementary Data 2) using previously published information[39] pertaining to the calving of iceberg A-38 that year. The calving of this iceberg was first observed by the US Defence Meteorological Satellite Programme's Operational Linescan System, and the iceberg had an areal extent upon calving of ~5600 km^2 (see also Supplementary Discussion 2).

Grounding-line location (GLL)

The location of the grounding line, where terrestrial ice detaches from its bed and begins to float, can be determined with high spatial precision using double-difference interferometric synthetic aperture radar techniques (DInSAR)[43]. In lieu of any InSAR observations acquired around 2000, the 1994, 1995 and 1996 GLLs used in this study (Figure 1; Extended Data Figures 1 and 2) are from previously published research applying DInSAR to ERS-1/2 Single-Look Complex (SLC) images with temporal baselines of either 1 day (1995, 1996) or 3 days (1994)[44]. These GLLs were acquired from https://nsidc.org/data/nsidc-0498.

The 2016/2017 GLLs, which over Larsen C Ice Shelf were acquired prior to the calving of iceberg A-68, were derived using similar techniques applied to Sentinel-1A/B Level-1 IW SLC images acquired in Terrain Observation by Progressive Scans (TOPS) mode and with a temporal baseline of 6-days. These GLLs were processed by the German Aerospace Center (Deutsches Zentrum für Luft- und Raumfahrt; DLR) as part of the ESA Antarctic Ice Sheet Climate Change Initiative (AIS CCI; http://esa-icesheets-antarctica-cci.org/).

The 2019 GLLs over Larsen C Ice Shelf and its surrounds were derived in this study from the same technique applied to Sentinel-1A/B SLC TOPS imagery acquired in 2019 (Supplementary Data 1). Data were obtained from the ASF as per our GRD imagery. We generated interferograms from all consecutive 6-day repeat-pass images acquired during austral winter and early springtime (June, July, August, and September) only, in order to minimise the potential for phase decorrelation associated with summertime surface warming and/or meltwater presence[25,45]. To maximize image co-registration accuracy (and, ultimately, phase coherence) in areas of sub-swath azimuthal overlap associated with the TOPS imaging mode, we applied an enhanced spectral diversity algorithm[46] to each interferometric image pair. Assuming the horizontal flow of ice to be common between each 6-day SAR image acquisition, we then removed phase effects due to surface topography in our interferograms using the REMA digital elevation model[40], and differenced all possible combinations of interferograms to reveal the grounding line. We identify the grounding line as the landward limit of closely spaced interferometric fringes present on double-difference interferograms, which represents the limit of tidally induced vertical flexure across the ice-sheet-shelf grounding zone[43,47]. Along with other remotely sensed components of the grounding zone[47-49], this location acts as a reliable proxy for the true grounding line, which cannot be imaged directly from satellite observations. Following ref. 50, we consider the positional uncertainty of all InSAR-derived GLLs examined in this study to be equivalent to one ice thickness or better, as constrained by a recent continent-wide ice thickness compilation[51].

Grounding-line location change

We mapped the GLL over Larsen C Ice Shelf from all austral winter and early springtime 2019 double-difference interferograms in order to: a) map the grounding line under a range of tidal amplitudes, and b) identify the absolute (high-tide) limit of tidal flexure, which can be used to deduce grounding-line migration more accurately over longer timescales[52]. Contrary to our 2019 mappings, the DLR AIS CCI 2016/2017 GLL product comprises only a single grounding line along the majority of Larsen C, which we assume represents a location on or close to the 2016/2017 high-tide limit of flexure. This is confirmed by an analysis of CATS2008a tide model output[53] proximal to the grounding zone (not shown) for the 2016/2017 imaging periods used to generate the AIS CCI interferograms.

Using this information, the relative change in GLL between 2017/2016 and 2019 along Larsen C's fastest-flowing tributary glaciers (Extended Data Figures 1 and 2) were approximated as follows. The grounding line of each glacier was assumed to have retreated if: a) the most landward 2019 GLL position resided greater than one centreline ice thickness at the grounding zone[51] away from the 2016/2017 position, and b) all 2019 GLLs along its centreline were situated landward of the 2016/2017 GLL. Glaciers were similarly assumed to have advanced if the opposite criteria were met. If mapped 2019 GLLs were observed both seaward and landward or within one centreline ice thickness of the 2016/2017 location, the glacier was assumed to have undergone negligible longer-term (i.e., non-tidal-state-induced) change. The same criteria were applied in our analysis of GLL change between the mid-1990s and 2016/7 (Extended Data Figures 1 and 2; no significant change detected) and we note that, due to a lack of Sentinel-1A/B image acquisitions poleward of ~78°S, no recent GLL observations or change analyses were performed over Ronne Ice Shelf. Given the colossal size of this ice shelf and its many pinning points, however, we do not expect this ice shelf to have undergone significant GLL change over the observational record.

Ice surface velocity change

To supplement our GLL analyses, we investigated recent changes in ice flow over the EAP using two newly available Antarctic annual ice velocity mosaics (Extended Data Figure 3). Spanning 2016 and 2018[54], these mosaics were generated from the error-weighted average of all image-pair velocity fields that have a centre date that fell within each year[54-55], and were acquired free of charge from the NASA ITS_LIVE data repository (https://its-live.jpl.nasa.gov/). Both mosaics are gridded at 240 m, and provide a critical update to the earlier velocity measurements documented in ref. 21. That is, the period 2016-2018 spans the calving of giant iceberg A-68 from Larsen C Ice Shelf (July 2017; Figure 1), and so allows for an analysis of post-breakaway upstream ice dynamical response. At time of writing, no publicly available annual mosaic exists for 2019.

Sea-ice concentration

The sea-ice concentration (SIC) records presented in Figures 2 and 3 and Extended Data Figures 5, 7, 9 and 10 are derived from monthly-mean-of-daily-mean Nimbus-7 SMMR and DMSP SSM/I-SSMIS satellite passive microwave observations[56] spanning January 1979 to December 2019. These data were acquired from the U.S. National Snow and Ice Data Center (NSIDC; https://nsidc.org/data/nsidc-0051) and are provided on a 25x25 km grid. Prior to analysis, we linearly interpolated data gaps in the observational record (December 1987 and January 1988), and excised all SIC records falling below 15% in line with NSIDC recommendations[57]. In Figure 3 and Extended Data Figure 5, the year 2003 was chosen as the start point of our anomaly calculations since it reflects: a) the first full year post-collapse of Larsen B Ice Shelf in 2002 and, b) the transition to persistently cool (negative IPO) conditions following the relatively warm (positive IPO) climatic conditions dominating the EAP between *c.* 1982-2002 (see Extended Data Figure 4, Supplementary Discussion 3 and the following section for further information).

To supplement our regional sea-ice observations, we also investigated changes in landfast sea ice fringing the EAP coastline, which may be poorly sampled by the coarse resolution of the passive microwave observations detailed above. This examination is warranted given the important role that landfast sea ice has played in the stability (or otherwise) of glacial ice (including ice shelves) in both Antarctica and the Arctic[27,58-64]. To do this, we used a new, comprehensive database of satellite-derived circum-Antarctic landfast sea-ice presence spanning 2000 to 2018[65]. Records contained in this database are corrected for the effects of migrating ice-shelf fronts to avoid the inadvertent misattribution of advanced shelf ice as landfast sea ice[65]. Similar to ref. 66, we generated grids of mean landfast sea-occurrence and its linear trend over all complete extended wintertime cycles (April-October) between 2002 and 2017, inclusive (Extended Data Figure 6). Extended wintertime months were analysed to obtain an impression of maximum landfast sea-ice presence over the majority of each year, which, by implication, represents a proxy for maximum ice-shelf buttressing afforded by landfast sea ice. No routine, high resolution records of landfast sea ice presence exist prior to 2000.

EAP Climatology

Our total precipitation, 2 m temperature and 10 m wind datasets (Figure 3; Extended Data Figures 4, 9 and 10; Supplementary Figure 1) were derived from the European Center for Medium-range Weather Forecast's (ECWMF) ERA5 global climate reanalysis[67], which, as a successor to ERA-Interim[68], is considered to provide the most accurate depiction of recent climatic conditions over coastal Antarctica[24,69]. We used finalized monthly-mean-of-daily-mean ERA5 data on single levels from January 1979 to December 2019, which are available from the Copernicus Climate Change Service Datastore (https://cds.climate.copernicus.eu/cdsapp#!/home) and have a horizontal resolution of 31x31 km (~0.28°x0.28°). At time of writing, no finalized ERA5 data exist prior to 1979. The anomaly maps presented in Figure 3, Extended Data Figure 4 and Supplementary Figure 1 were calculated in the same way as for sea ice concentration analyses.

Ocean wave data

To investigate historical ocean wave conditions along the EAP coastline, we examined ERA5 3-hourly records of peak wave period and significant wave height of combined wind waves and swell for all months in which the satellite passive microwave record revealed extensive open-water conditions seaward of the EAP's ice shelves (Extended Data Figure 7). These records, gridded at 0.5°x0.5° resolution, are derived from the global ocean wave model used in the ECMWF's Integrated Forecasting System (IFS) which: a) is parameterised to account for the influence of sea ice (all wave model cells where SIC>30% are set to 'no data') and, b) has recently been updated to improve the global accuracy of the most common ocean variables, including significant wave height[70]. Since 1991, routine wave height observations from satellite radar altimeters have also been assimilated into the model[67], offering additional constraints on wave geometry in the polar oceans where in-situ wind observations are limited. Refs. 67 and 71 provide further information on the ocean wave model and its data assimilation strategies.

To examine the impact of ocean waves on ice-shelf flexure during each 'open ocean year', we generated timeseries of peak wave period and significant wave height for all waves travelling towards the Larsen A, B and C ice shelves with an incidence angle of between 30° E and 90° E off the coast (Extended Data Figure 7). For the area encompassing the New Bedford, Wright-Keller and Ronne ice shelves, an incidence range of 30-155° E was used. Following ref. 27, these limits represent the conservative direction of open-ocean 'pathways' identifiable in the passive microwave sea ice record (Extended Data Figure 7), from which ocean waves will have reached the ice front. These timeseries were then compared with the idealised model results of ref. 27 to deduce the influence of observed wave height and period on ice-shelf frontal strain.

Sea-surface slope data

The sea-surface slope information presented in Extended Data Figure 8 was derived from 3-hourly Hybrid Coordinate Ocean Model (HYCOM[72-73]) reanalysis outputs of anomalous sea-surface height. We used GOFS 3.0 and 3.1 outputs from experiments GLBu0.08/expt_19.1, and GLBy0.08_expt_93.0 in our analyses, respectively, which provide sea-surface height anomaly estimates at a resolution of 0.04°x0.08° over the Southern Ocean. Given the sparse coverage of in-situ sea-surface records in the Weddell Sea, we only use outputs since November 2000, from which time operational satellite radar altimeter-derived observations of sea-surface height are assimilated into the model[73-75]. Sea-surface height outputs are freely available at: https://www.hycom.org/hycom, and sea-surface slopes were ascertained on a pixel-wise basis from all neighbouring pixels using conventional techniques[76]. In Extended Data Figure 8, the high frequency, low amplitude variability superimposed upon the timeseries corresponds primarily to a convolution of changes in ocean tidal height, atmospheric pressure (inverse barometer effect) and, presumably, pack ice freeboard as detected by satellite radar altimetry.

Interdecadal Pacific Oscillation and Southern Annular Mode

The Interdecadal Pacific Oscillation (IPO) timeseries shown in Extended Data Figure 4 was acquired from the National Oceanic and Atmospheric Administration's Physical Sciences Laboratory (https://psl.noaa.gov/data/timeseries/IPOTPI/), and represents Tripole Index for the Interdecadal Pacific Oscillation (TPI (IPO)) values derived from the UK Met Office Hadley Centre's Sea Ice and Sea Surface Temperature (SST) dataset 1.1. (HADISST1.1). This dataset contains global monthly SST and SIC fields on a 1°x1° grid from 1870 to present, from which monthly TPI (IPO) values were calculated based on the difference between SST anomalies averaged over the central equatorial Pacific and in the Northwest and Southwest Pacific (after ref. 77).

The Southern Annular Mode (SAM) timeseries presented in Extended Data Figure 4 was calculated by G. Marshall at the British Antarctic Survey and is freely available at: https://legacy.bas.ac.uk/met/gjma/sam.html. This dataset is derived from the station-based observations detailed in ref. 78 and is based on the zonal pressure difference between 40°S and 65°S.

Figure Generation

Figure 3, Extended Data Figures 4-10 and Supplementary Figure 1 were generated partly using the data analysis and visualization functions detailed in refs. 79-80.

Data Availability: All satellite and climate reanalysis datasets utilized in this study are publicly available and can be obtained from the data repositories detailed in the Methods section. The CATS2008a tidal model is available at: https://www.usap-dc.org/view/dataset/601235, and the ice front and 2019 grounding line location files generated in this study are available at https://doi.org/10.17863/CAM.54490 (ref. 81) and https://doi.org/10.17863/CAM.54489 (ref. 82), respectively. Supplementary Data 1 contains a list of all satellite images used in the production of the of our ice front and grounding line datasets, and Supplementary Data 2 contains the ice-shelf areal extent values used in the production of Figure 2.

Code Availability

The MATLAB codes developed for this study are available upon request to the corresponding author.

Methods References

(38) Cook, A. J., Fox, A. J., Vaughan, D. G. & Ferrigno, J. G. Retreating Glacier Fronts on the Antarctic Peninsula over the Past Half-Century. *Science* **308(5721)**, 541–544 (2005). doi: 10.1126/science.1104235.

(39) Ferrigno, J. G., Foley, K. M., Swithinbank, C., Williams Jr., R. C. & Dailide, L. M. Coastal-change and glaciological map of the Ronne Ice Shelf area, Antarctica: 1974–2002 (to accompany MAP I–2600–D), U.S. Department of the Interior, United States Geological Survey (2005). doi:10.3133/i2600D.

(40) Howat, I. M., Porter, C., Smith, B. E., Noh, M-J. & Morin, P. The Reference Elevation Model of Antarctica. *Cryosphere* **13**, 665–674 (2019). doi:10.5194/tc-13-665-2019.

(41) Depoorter, M. A. *et al*. Calving fluxes and basal melt rates of Antarctic ice shelves. *Nature* **502**, 89–92 (2013). doi:10.1038/nature12567.

(42) Budge, J. S. & Long, D. G. A Comprehensive Database for Antarctic Iceberg Tracking Using Scatterometer Data. *IEEE J. Sel. Top. Appl. Earth. Obs. Remote Sens.* **11(2)**, 434–442 (2018). doi:10.1109/JSTARS.2017.2784186.

(43) Rignot, E., Mouginot, J. & Scheuchl, B. Antarctic grounding line mapping from differential satellite radar interferometry. *Geophys. Res. Lett.* **38(10)**, L10504 (2011). doi:10.1029/2011GL047109.

(44) Rignot, E., Mouginot, J. & Scheuchl, B. MEaSUREs Antarctic Grounding Line from Differential Satellite Radar Interferometry, Version 2. Boulder, Colorado USA. NASA National Snow and Ice Data Center Distributed Active Archive Center (2016). doi:10.5067/IKBWW4RYHF1Q.

(45) Luckman, A. *et al*. Surface melt and ponding on Larsen C Ice Shelf and the impact of föhn winds. *Antarct. Sci.* **26(6)**, 625–635 (2014). doi:10.1017/S0954102014000339.

(46) Yague-Martinez, N. *et al*. Interferometric Processing of Sentinel-1 TOPS Data. *IEEE Trans. Geosci. Remote Sens.* **54(4)**, 2220–2234 (2016). doi:10.1109/TGRS.2015.2497902.

(47) Christie, F. D. W., Bingham, R. G., Gourmelen, N., Tett, S. F. B. & Muto, A. Four-decade record of pervasive grounding line retreat along the Bellingshausen margin of West Antarctica, *Geophys. Res. Lett.* **43**, 5741–5749 (2016). doi:10.1002/2016GL068972.

(48) Fricker, H. A. *et al*. Mapping the grounding zone of the Amery Ice Shelf, East Antarctica using InSAR, MODIS and ICESat. *Antarct. Sci.* **21(05)**, 515–532 (2009). doi: 10.1017/S095410200999023X.

(49) Christie, F. D. W. *et al*. Glacier change along West Antarctica's Marie Byrd Land Sector and links to inter-decadal atmosphere–ocean variability. *Cryosphere* **12**, 2461–2479 (2018). doi: 10.5194/tc-12-2461-2018.

(50) Rack, W., King, M. A., Marsh, O. J., Wild, C. T. & Floricioiu, D. Analysis of ice shelf flexure and its InSAR representation in the grounding zone of the southern McMurdo Ice Shelf. *Cryosphere* **11(6)**, 2481–2490 (2017). doi:10.5194/tc-11-2481-2017.

(51) Morlighem, M., *et al.* Deep glacial troughs and stabilizing ridges unveiled beneath the margins of the Antarctic ice sheet. *Nat. Geosci.* **13**, 132–137 (2020). doi:10.1038/s41561-019-0510-8.

(52) Milillo, P. *et al*. On the Short-term Grounding Zone Dynamics of Pine Island Glacier, West Antarctica, Observed With COSMO-SkyMed Interferometric Data, *Geophys. Res. Lett.* **44(20)**, 10436–10444 (2017). doi: 10.1002/2017GL074320.

(53) Padman, L., Fricker, H. A., Coleman, R., Howard, S. & Erofeeva, S. A new tidal model for the Antarctic ice shelves and seas. *Ann. Glaciol.* **34**, 247–254 (2002, updated 2008).

(54) Gardner, A. S., Fahnestock, M. A. & Scambos, T. A. ITS_LIVE Regional Glacier and Ice Sheet Surface Velocities. Data archived at National Snow and Ice Data Center (2019). doi:10.5067/6II6VW8LLWJ7.

(55) Gardner, A. S. *et al*. Increased West Antarctic and unchanged East Antarctic ice discharge over the last 7 years. *Cryosphere* **12(2)**, 521–547 (2018). doi:10.5194/tc-12-521-2018.

(56) Cavalieri, D. J., Parkinson, C. L., Gloersen, P. & Zwally, H. J. Sea Ice Concentrations from Nimbus-7 SMMR and DMSP SSM/I-SSMIS Passive Microwave Data, Version 1. Boulder, Colorado USA. NASA National Snow and Ice Data Center Distributed Active Archive Center (1996, updated 2020). doi:10.5067/8GQ8LZQVL0VL.

(57) Fetterer, F., Knowles, K., Meier, W. N., Savoie, M. & Windnagel, A. K. Sea Ice Index, Version 3. Boulder, Colorado USA. NSIDC: National Snow and Ice Data Center (2017, updated 2020). doi:10.7265/N5K072F8.

(58) Todd, J. & Christoffersen, P. Are seasonal calving dynamics forced by buttressing from ice mélange or undercutting by melting? Outcomes from full-Stokes simulations of Store Glacier, West Greenland. *Cryosphere*, **8**, 2353–2365 (2014). doi:10.5194/tc-8-2353-2014.

(59) Carr, J. R., Stokes, C., & Vieli, A. Recent retreat of major outlet glaciers on Novaya Zemlya, Russian Arctic, influenced by fjord geometry and sea-ice conditions. *J. Glaciol.* **60(219)**, 155–170 (2014). doi:10.3189/2014JoG13J122.

(60) Greene, C. A. et al. Seasonal dynamics of Totten Ice Shelf controlled by sea ice buttressing. *Cryosphere* **12**, 2869–2882 (2018). doi:10.5194/tc-12-2869-2018.

(61) Liang, Q. et al. Ice flow variations at Polar Record Glacier, East Antarctica. *J. Glaciol.* **65(250)**, 279–287 (2019). doi:10.1017/jog.2019.6.

(62) Aoki, S. Breakup of land-fast sea ice in Lützow-Holm Bay, East Antarctica, and its teleconnection to tropical Pacific sea surface temperatures, *Geophys. Res. Lett.* **44(7)**, 3219–3227 (2017). doi:10.1002/2017GL072835.

(63) Fraser, A. D., et al. East Antarctic Landfast Sea Ice Distribution and Variability, 2000–08. *J. Clim.* **25(4)**, 1137–1156 (2012). doi:10.1175/JCLI-D-10-05032.1.

(64) Robel, A. A. Thinning sea ice weakens buttressing force of iceberg mélange and promotes calving. *Nat. Comms.* **8**, 14596 (2017). doi:10.1038/ncomms14596.

(65) Fraser, A. D., *et al*. High-resolution mapping of circum-Antarctic landfast sea ice distribution, 2000–2018. *ESSD* **12**, 2987–2999 (2020). Doi:10.5194/essd-12-2987-2020.

(66) Nihashi, S. & Ohshima, K. I. Circumpolar Mapping of Antarctic Coastal Polynyas and Landfast Sea Ice: Relationship and Variability. *J. Clim.* **28(9)**, 3650–3670 (2015). doi:10.1175/JCLI-D-14-00369.1.

(67) Hersbach, H. et al. The ERA5 global reanalysis. *Q. J. R. Meteorol. Soc.* **146**, 1999–2049 (2020). doi:10.1002/qj.3803.

(68) Dee, D. P. *et al*. The ERA-Interim reanalysis: configuration and performance of the data assimilation system. *Q. J. R. Meteorol. Soc.* **137**, 553–597 (2011). doi:10.1002/qj.828.

(69) Dong, X., Wang, Y., Hou, S., Ding, M., Yin, B. & Zhang, Y. Robustness of the Recent Global Atmospheric Reanalyses for Antarctic Near-Surface Wind Speed Climatology. *J. Clim.* **33(10)**, 4027–4043. doi:10.1175/JCLI-D-19-0648.1.

(70) Bidlot, J-R. Model upgrade improves ocean wave forecasts. *ECMWF Newsletter* **159** (2019). https://www.ecmwf.int/en/newsletter/159/news/model-upgrade-improves-ocean-wave-forecasts.

(71) ECWMF. Part VII: ECMWF Wave Model in *IFS documentation – Cy43r3 Operational implementation 11 July 2017* (2017). https://www.ecmwf.int/sites/default/files/elibrary/2017/17739-part-vii-ecmwf-wave-model.pdf.

(72) Chassignet, E. P. *et al.* The HYCOM (HYbrid Coordinate Ocean Model) data assimilative system. *J. Mar. Syst.* **65**, 60-83 (2007). doi:10. 1016/j.jmarsys.2005.09.016.

(73) Cummings, J.A. & Smedstad, O. M. *Variational Data Assimilation for the Global Ocean* (Chapter 13) in Park, S.K. & Xu, L. (eds)., *Data Assimilation for Atmospheric, Oceanic and Hydrologic Applications* **2**, Springer-Verlag Berlin Heidelberg (2013). doi:10.1007/978-3-642-35088-7 13.

(74) Brenner, A. C., DiMarzio, J. P., & Zwally, H. J. *GFO NASA/GSFC Polar Ice Data Processing and Validation Report* (2001). https://icesat4.gsfc.nasa.gov/missions/gfo_cal_val.php

(75) Cummings, J. A. Operational multivariate ocean data assimilation. *Q. J. R. Meteorol. Soc.* **131**, 3583-3607 (2005). doi: 10.1256/qj.05.105.

(76) Burrough, P. A., & McDonnell, R. A. *Principles of Geographical Information Systems*, Oxford University Press, New York, 190 pp. (1998).

(77) Henley, B. J. *et al*. A Tripole Index for the Interdecadal Pacific Oscillation. *Clim. Dyn.* **45**, 3077–3090 (2015). doi:10.1007/s00382-015-2525-1.

(78) Marshall, G. J. Trends in the Southern Annular Mode from Observations and Reanalyses. *J. Clim.* **16(24)**, 4134–4143 (2003). doi:10.1175/1520-0442(2003)016<4134:TITSAM>2.0.CO;2.

(79) Greene, C. A., Gwyther, D. E. & Blankenship, D. D. Antarctic Mapping Tools for MATLAB. *Comput. Geosci.* **104**, 151–157 (2017). doi:10.1016/j.cageo.2016.08.003.

(80) Greene, C. A. *et al*. The Climate Data Toolbox for MATLAB. *Geochem. Geophys.* **20(7)**, 3774–3781 (2019). doi:10.1029/2019GC008392.

(81) Christie, F. D. W., Benham, T. J., Batchelor, C. L., Rack, W., Montelli, A., & Dowdeswell, J. A. Antarctic Ice Front positions, 1979-2021, supporting "*Antarctic ice-shelf advance driven by anomalous atmospheric and sea-ice circulation*". Cambridge Apollo. doi:10.17863/CAM.54490 (2022a).

(82) Christie, F. D. W., Benham, T. J., Batchelor, C. L., Rack, W., Montelli, A., & Dowdeswell, J. A. Antarctic Grounding Line Location from Sentinel-1A/B double-difference interferometry, 2019, supporting "*Antarctic ice-shelf advance driven by anomalous atmospheric and sea-ice circulation*". Cambridge Apollo. doi:10.17863/CAM.54489 (2022b).

(83) Rignot, E., Mouginot, J. & Scheuchl, B. *MEaSUREs InSAR-Based Antarctica Ice Velocity Map, Version 2*. Boulder, Colorado USA. NASA National Snow and Ice Data Center Distributed Active Archive Center (2017). doi:10.5067/D7GK8F5J8M8R.

(84) Mouginot, J., Scheuchl, B. & Rignot, E. *MEaSUREs Antarctic Boundaries for IPY 2007-2009 from Satellite Radar, Version 2*. Boulder, Colorado USA. NASA National Snow and Ice Data Center Distributed Active Archive Center (2017). doi:10.5067/AXE4121732AD.

Extended Data

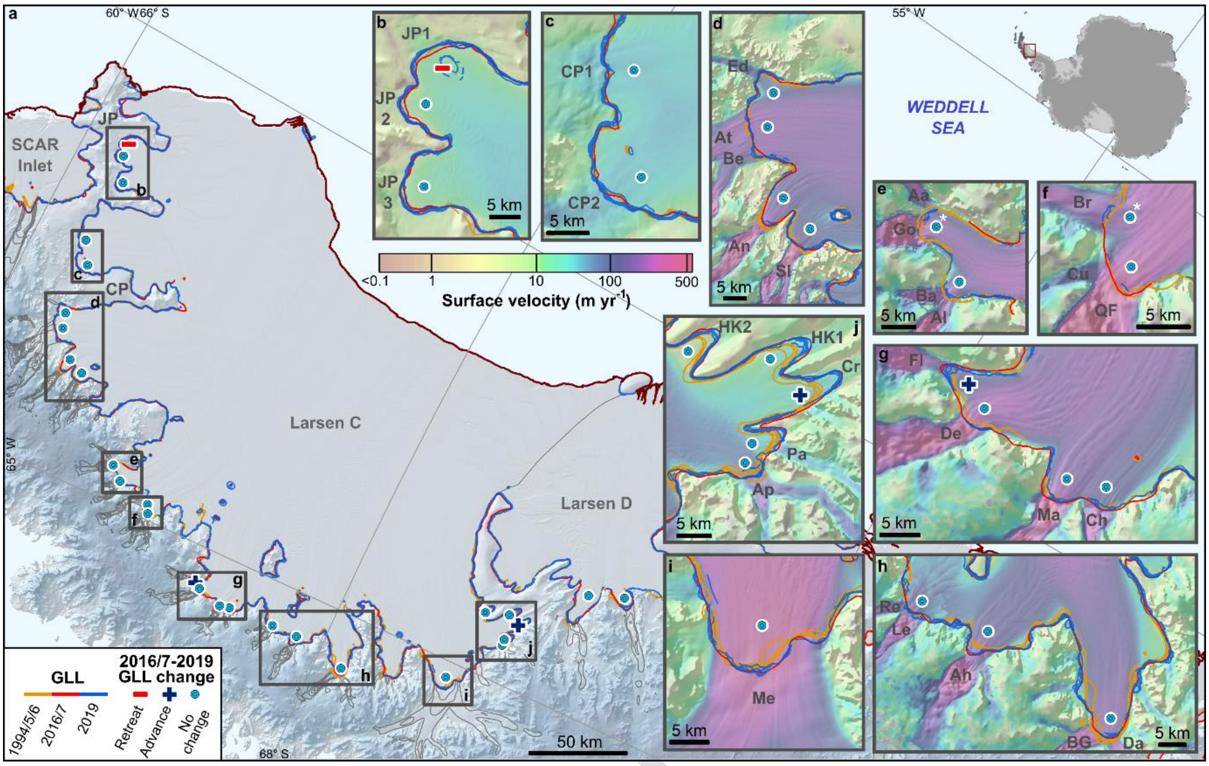

Extended Data Figure 1 | Grounding-line migration along Larsen C Ice Shelf. ***a***, Change in grounding line location (GLL) between 1994-6, 2016-7 and 2019 as determined from satellite radar-based techniques (Methods). Following Figure 1, symbols denoting recent (2016/7-2019) GLL change are also shown, as well as the position of the 2019 ice front (maroon) and ice surface velocity contours[83] (100 m yr^{-1} increments) over grounded ice. ***b-j***, spatial extent of GLL change across the regions labelled in ***a***, superimposed over recent ice surface velocity magnitudes[83]. *JP1-3* denote unnamed glaciers 1-3 draining from Jason Peninsula; *CP1-2*, unnamed glaciers 1-2 draining from Churchill Peninsula; *At*, Atlee; *Be*, Bevin; *An*, Anderson; *Sl*, Sleipnir; *Aa*, Aagaard; *Go*, Gould; *Ba*, Balch; *Al*, Alberts; *Br*, Breitfus; *Cu*, Cumpston; *QF*, Quartermain-Fricker; *Fl*, Flint; *De*, Demorest; *Ma*, Matthes; *Ch*, Chamberlain; *Re*, Renaud; *Le*, Lewis; *Ah*, Ahlmann; *BG*, Bill's Gulch; *Da*, Daspit; *Me*, Mercator; *Ap*, Aphrodite; *Pa*, Pan and *Cr*, Cronus glaciers. *HK1-2* denotes the unnamed glaciers flowing from Hollick-Kenyon Peninsula. In ***e*** and ***f***, white asterisks denote no change since the mid-1990s in lieu of 2016/7 GLL coverage.

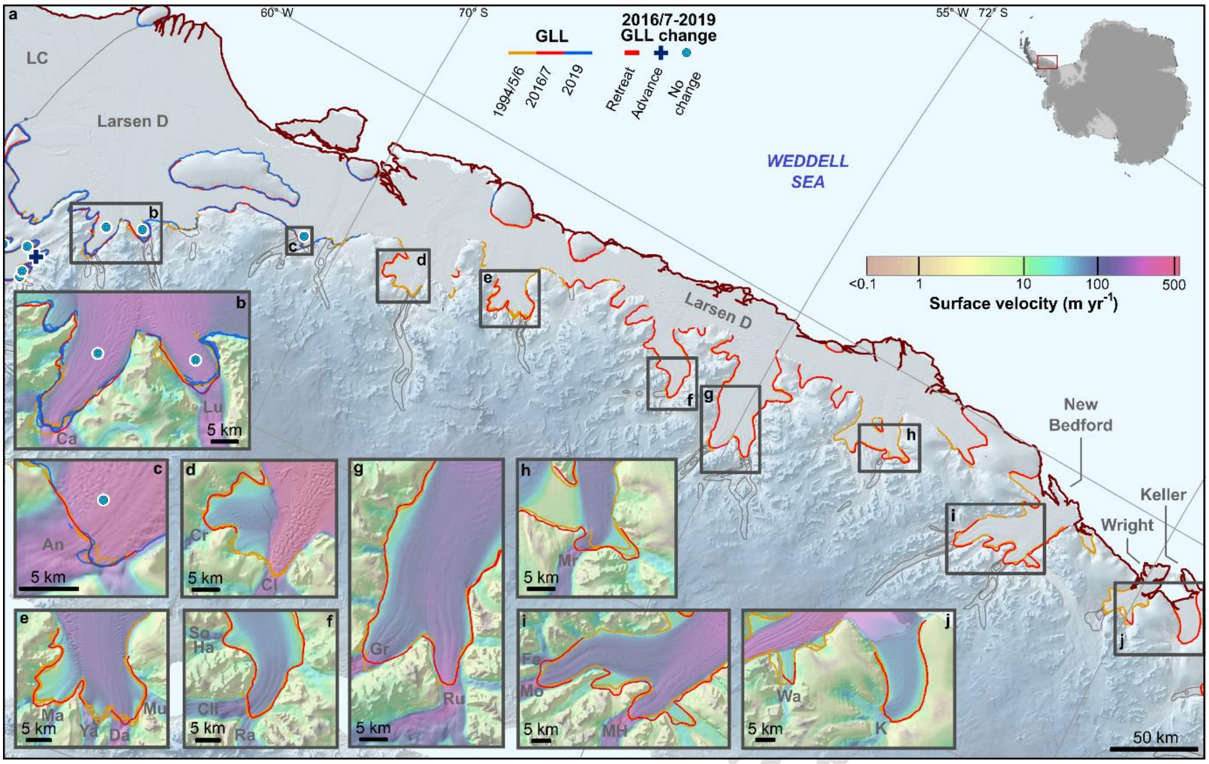

Extended Data Figure 2 | Grounding-line migration along Larsen D, New Bedford, Wright and Keller ice shelves' fastest-flowing glaciers. ***a***, Change in grounding line location (GLL) between 1994-6, 2016-7 and 2019 as determined from satellite radar-based techniques (Methods). Following Figure 1, symbols denoting recent (2016/7-2019) GLL change proximal to Larsen C Ice Shelf (LC) are also shown, as well as the position of the 2019 ice front (maroon) and ice surface velocity contours[83] (100 m yr^{-1} increments) over grounded ice. ***b-j***, spatial extent of GLL change across the regions labelled in ***a***, superimposed over recent ice surface velocity magnitudes[83]. *Ca* denotes Casey Glacier; *Lu*, Lurabee; *An*, Anthony; *Cr*, Croom; *Cl*, Clifford; *Ma*, Matheson; *Ya*, Yates; *Da*, Dana; *Mu*, Murrish; *So*, Soto; *Ha*, Haley; *Cli*, Cline; *Ra*, Rankin; *Gr*, Gruening; *Ru*, Runcorn; *Mr*, Maury; *Fe*, Fenton; *Mo*, Mosby; *MH*, Meinardus-Haines and *Wa*, Waverly glaciers. *K* denotes the unnamed glacier draining to Keller Inlet. All other abbreviations are the same as in Figure 1.

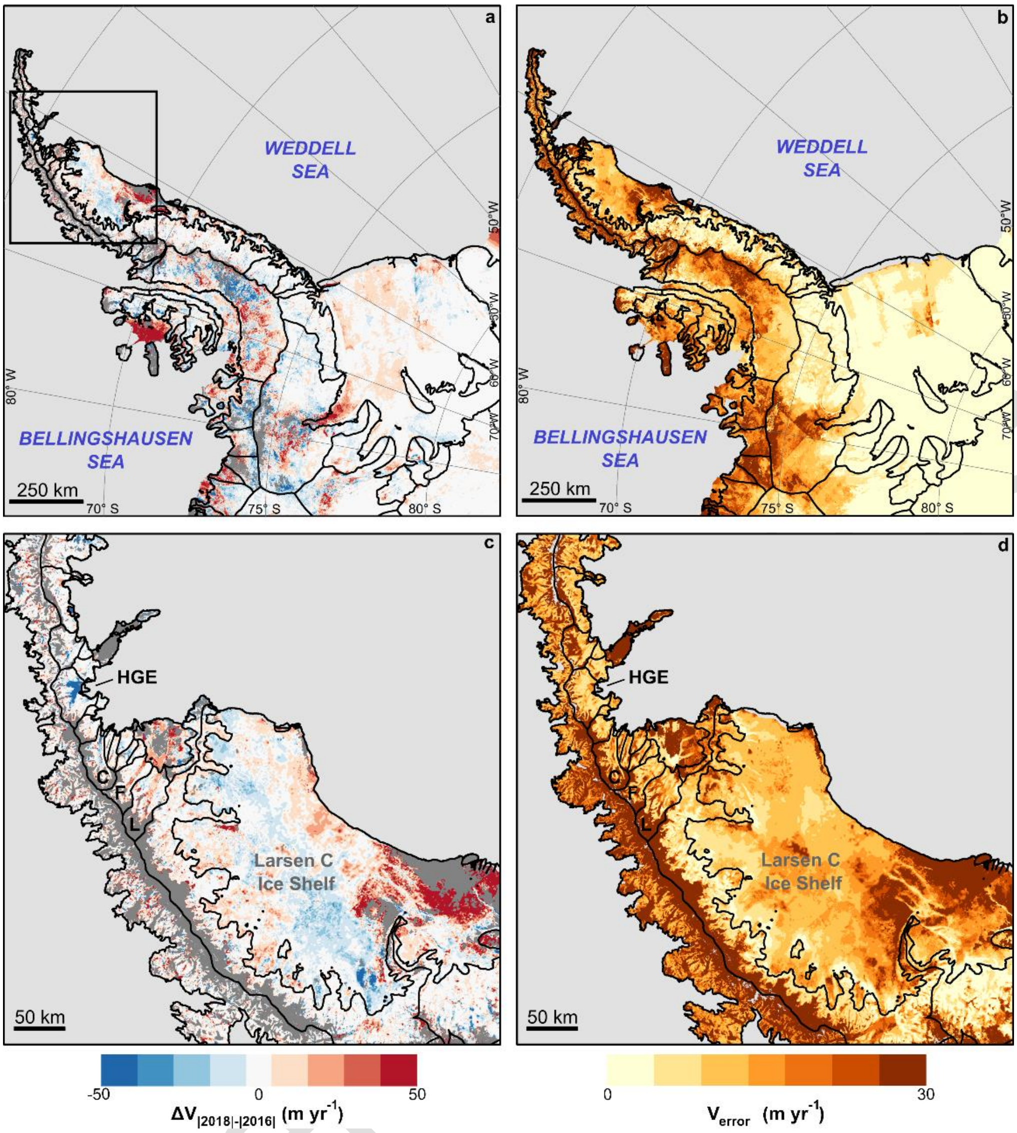

Extended Data Figure 3 | Recent changes in EAP ice-surface flow. ***a***, Landsat 8-derived velocity change between 2016 and 2018 over the Antarctic Peninsula region. Black lines delineate the ice drainage basins detailed in a recent study[84]. The 2018 ice front position is also shown. To minimise erroneous data coverage over ice divides and other regions of complex topography, data are masked (dark grey) where V_{error} exceeded 30 m yr^{-1} in either 2016 or 2018 (or both). Black box indicates the detail shown in ***c*** and ***d***. ***b***, Landsat 8-derived V_{error}. In ***c*** and ***d***, *HGE* denotes Hektoria, Green and Evans; *C*, Crane; *F*, Flask and *L*, Leppard glaciers. Note the continued dynamic acceleration of Flask and Leppard glaciers following the disintegration of Larsen B Ice Shelf in 2002, and the lack of any similar grounded ice-flow acceleration upstream of Larsen C Ice Shelf following the calving of iceberg A-68 (Figure 1).

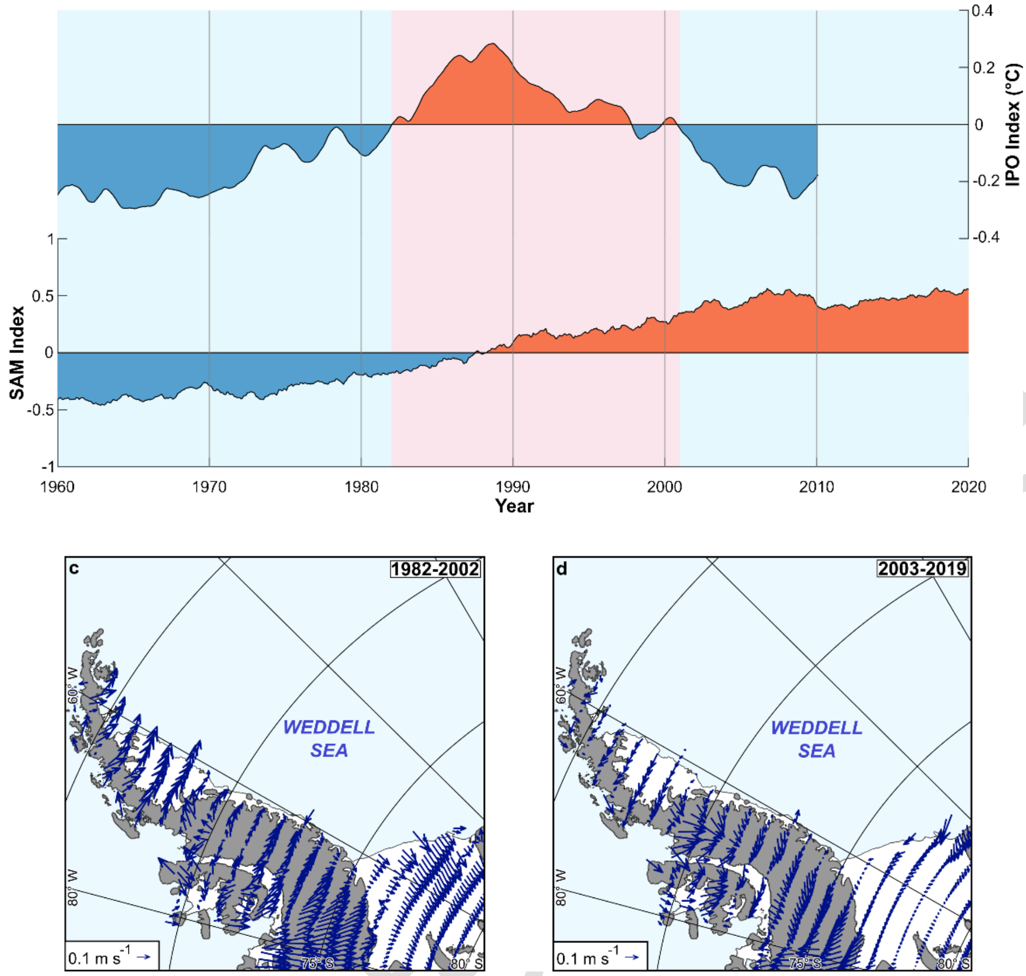

Extended Data Figure 4 | Wider climatic conditions over the Weddell Sea Sector. ***a*** and ***b***, Monthly changes in the Interdecadal Pacific Oscillation (IPO) and Southern Annular Mode (SAM), respectively (Methods). Data have been smoothed using a 20-year running mean to emphasise multi-decadal variability. Following Figure 2, blue (pink) shading denotes the approximate timing of relatively cool (warm) climatic conditions over the Antarctic Peninsula as deduced from (*a*). ***c*** and ***d***, annual-averaged 10 m wind anomalies over the Antarctic Peninsula Ice Sheet for the periods (***c***) January 1982 to December 2002 and (***d***) January 2003 to December 2019, respectively, relative to all months on record (1979-2019). Note the abrupt reversal in wind direction over most EAP ice shelves (except Ronne) between the two periods, indicative of reduced foehn wind-driven ice-shelf surface melting, calving and coastal sea-ice evacuation through time (see main text and Supplementary Discussion 3 for further information).

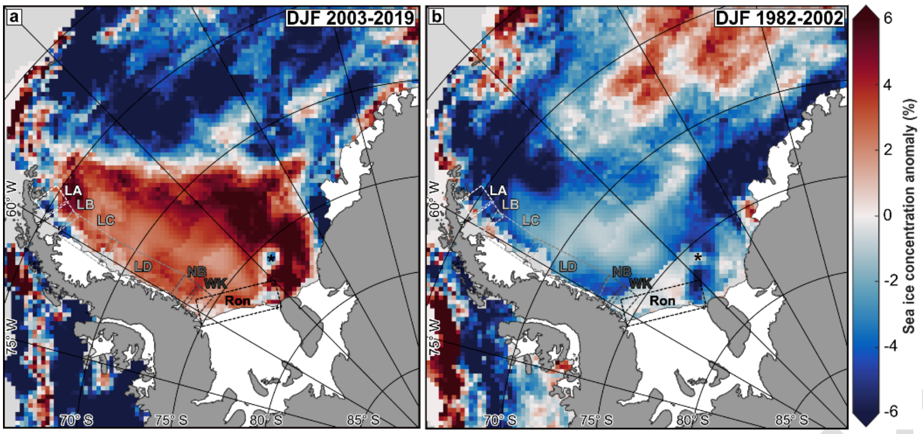

Extended Data Figure 5 | Austral summertime sea-ice conditions over the Weddell Sea Sector. ***a*** and ***b***, Mean passive microwave-derived sea-ice concentration anomalies for all complete austral summertime (DJF) cycles between 2003 and 2019 and 1982 and 2002, respectively, relative to all earlier, complete summertime cycles on record (1980-2019). Black asterisk denotes the approximate location of iceberg A-23a (lightly grounded at this location since 2000); light grey shading, no data. In both panels, dashed boxes indicate sea-ice averaging regions used in the production of Figure 2 and Extended Data Figures 9 and 10. Figure highlights the importance of summer sea ice variability in dominating the annual-averaged observations presented in Figure 3.

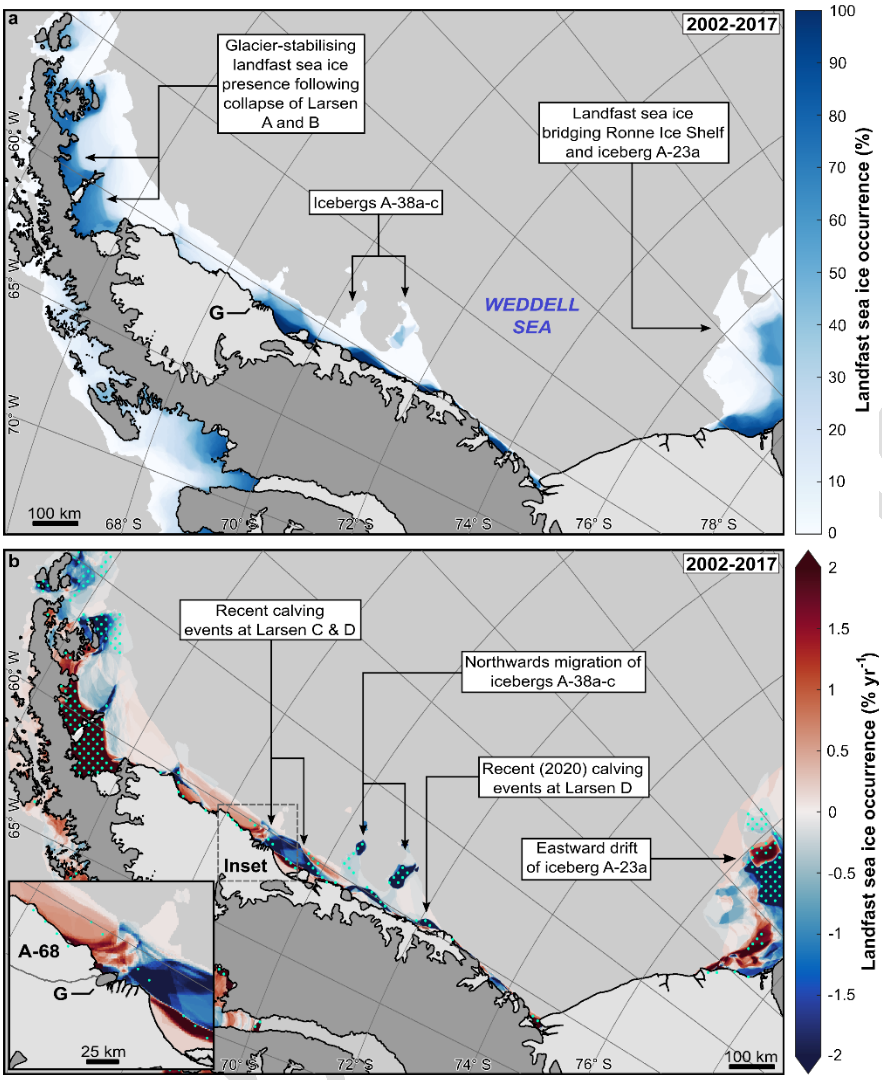

Extended Data Figure 6 | Landfast sea ice conditions in the eastern Antarctic Peninsula. ***a***, Mean extended wintertime (April to October) landfast sea ice occurrence offshore of the EAP, 2002-2017. 100% occurrence denotes permanent landfast sea-ice presence over the observational record during these months. *G* denotes Gipps Ice Rise. ***b***, Linear trend in extended wintertime landfast sea ice occurrence. Red denotes increased sea ice occurrence through time. Cyan stippling indicates statistically significant trends ($p<.1$) over the 18-year observational window, as determined from a two-tailed Pearson's Linear Correlation Coefficient test. Inset shows detail around Gipps Ice Rise, including near the rift that formed iceberg A-68 (dark grey line; see main text and Supplementary Discussion for further information).

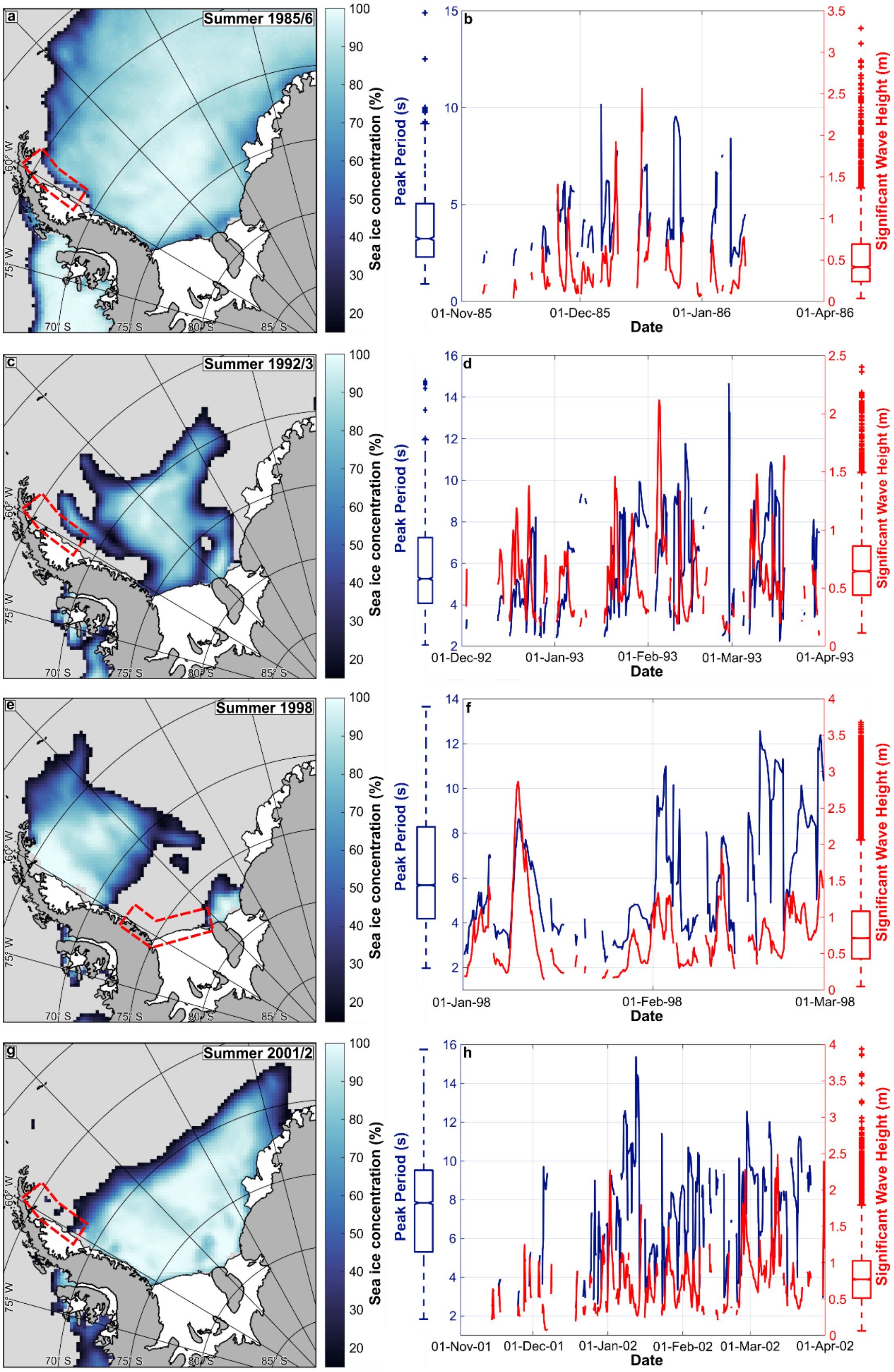

Extended Data Figure 7 | Caption overleaf.

Extended Data Figure 7 | EAP 'open ocean years', 1979-2019. ***a***,***c***,***e***,***g***, Monthly mean sea-ice minima observed during the 'open ocean years' indicated in Figure 2. Grey shading denotes <15% sea-ice concentration. Note that means overestimate sub-monthly sea ice extent and concentration, especially near the ice edge. ***b***,***d***,***f***,***h***, ERA5-derived timeseries showing corresponding ocean wave conditions (median peak period and significant height of combined wind waves and swell; see Methods) offshore of the Larsen A, B, C (panels *b*,*d*,*h*) and New Bedford, Wright, Keller and Ronne ice shelves (panel *f*). Median values were calculated from all cells in the red boxes shown in panels *a*,*c*,*e*,*g*, when ocean waves were incident upon the ice shelves. Times when waves were not incident are masked. Boxplots show the statistical distribution of observed wave conditions, with outliers (>1.5 times the interquartile range) marked as crosses.

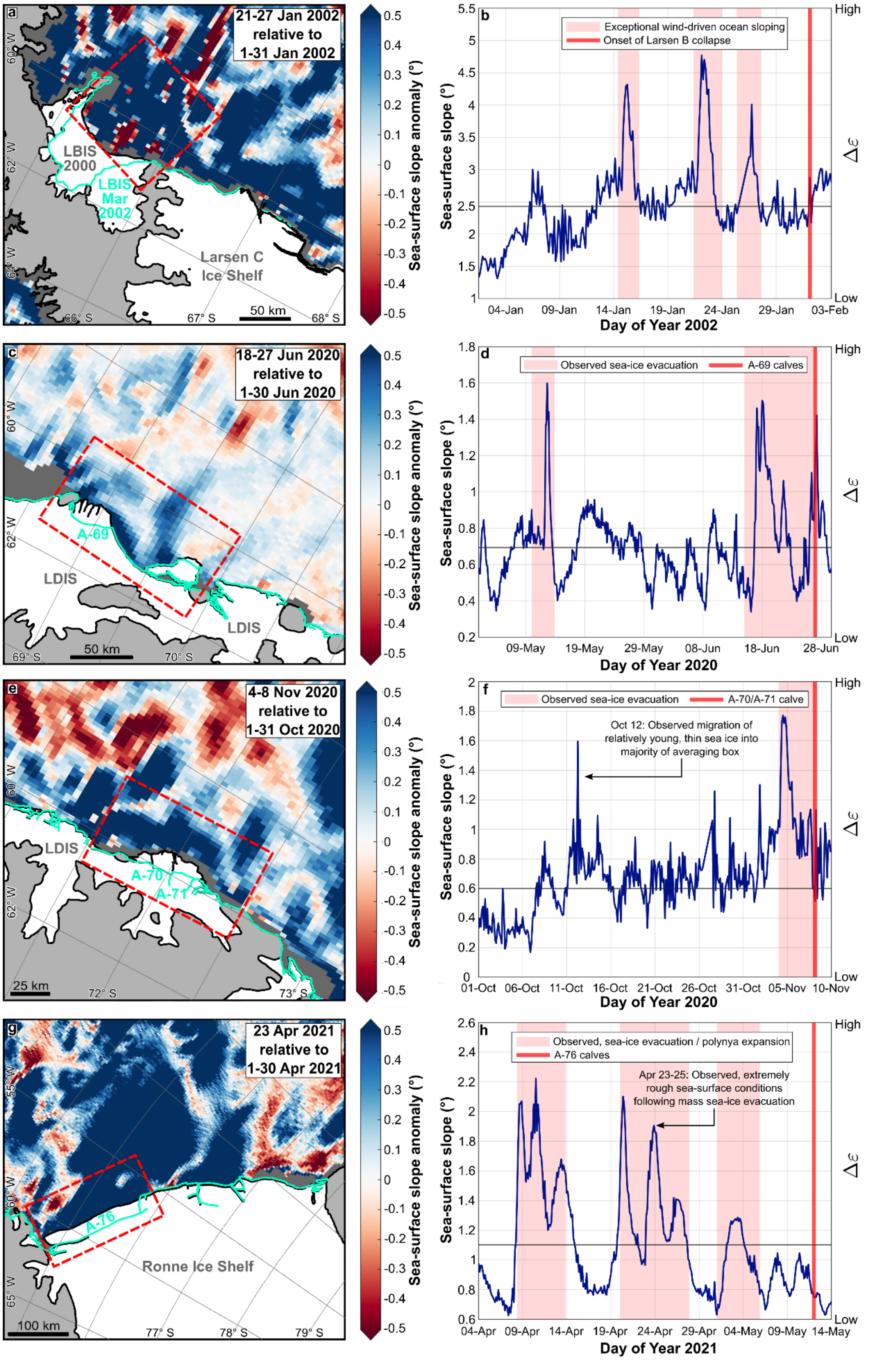

Extended Data Figure 8 | Caption overleaf.

Extended Data Figure 8 | Sea-surface slope conditions prior to ice-shelf frontal recession. ***a*,*c*,*e*,*g***, Mean HYCOM-derived sea-surface slope anomalies offshore of the Larsen B (LBIS), Larsen D (LDIS) and Ronne ice shelves prior to the collapse of Larsen B (*a*) and the calving of icebergs A-69 (*c*), A-70/71 (*e*), and A-76 (*g*). Temporal averaging window and baseline periods are indicated top right, the latter of which corresponds to mean sea-surface slope during the month of calving (October 2020 for *e* given the calving of A-70/71 in early November 2020). Black and cyan lines indicate pre- and post-recession location of the ice shelves, respectively. Dark grey denotes no data. ***b*,*d*,*f*,*h***, timeseries showing mean sea-surface slopes in the days and weeks prior to collapse (*b*) or calving (*d*,*f*,*h*), as averaged over the red dashed boxes shown in a,c,e,g. Vertical red lines denote the onset of collapse/calving; pink shading, periods of intense slopes following either exceptionally strong winds on the already open ocean (b) or observed, pronounced coastal sea-ice evacuation (d,f,h ; cf. Supplementary Videos 2-4). Horizontal grey lines indicate mean slope over the baseline periods shown in a,c,e,g. Relative change in ice-shelf frontal strain, Ɛ, corresponding to variations in slope are also shown (right-hand axes).

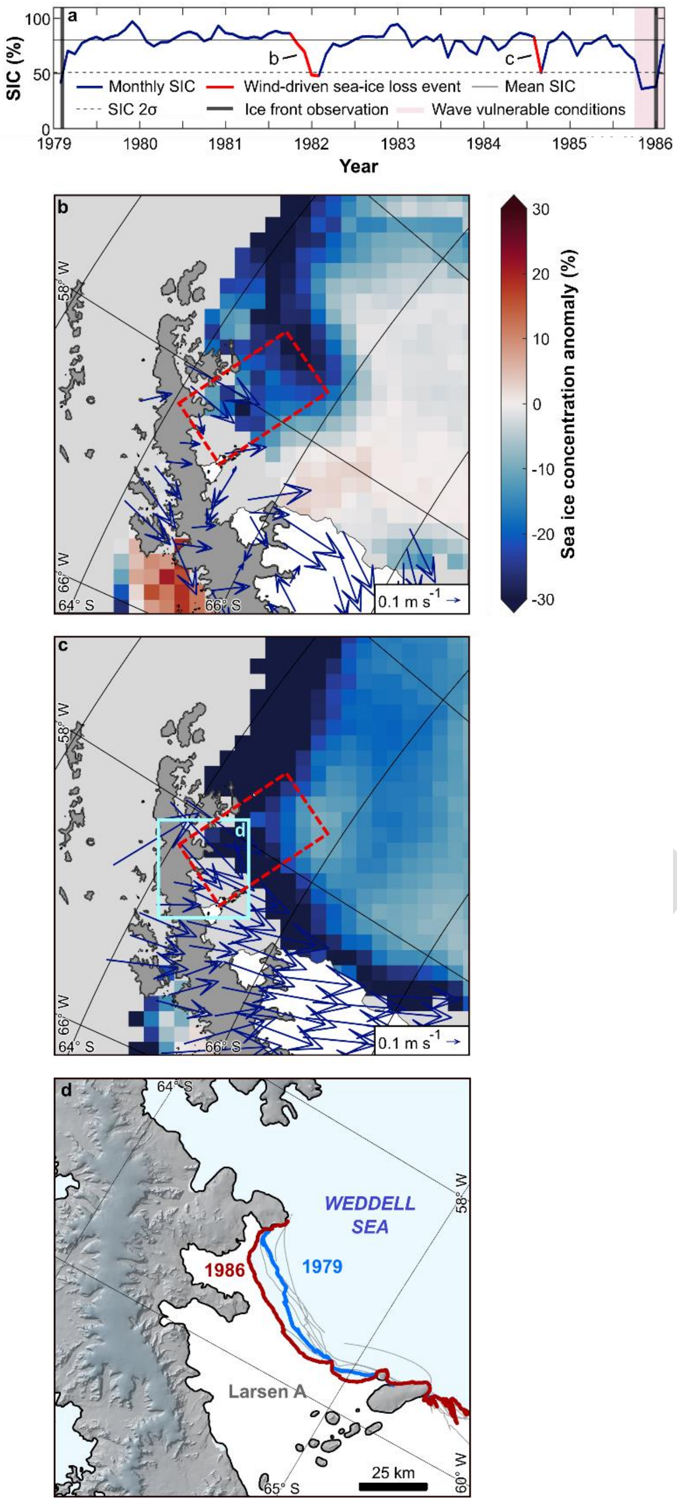

Extended Data Figure 9 | Larsen A coastal sea-ice variability. ***a***, Timeseries showing monthly SIC between 1979 and 1986 when a calving event of uncertain timing occurred (cf. Figure 2). Values represent the average of all cells contained in the red dashed box shown in *b*. Red lines denote times in which highly anomalous (>2σ), wind-driven coastal sea-ice losses would have rapidly de-buttressed Larsen A's ice front, prompted enhanced gravitational ice-shelf flow due to increased (oceanward-down) sea-surface slopes and likely initiated calving. Pink shading shows 'open ocean conditions' as in Figure 2. ***b*** and ***c***, mean wind (vector) and SIC (raster) anomalies during the times indicated by the red lines in *a* (1981/2 and 1984, respectively). Note the anomalous offshore direction of winds over Larsen A in both panels. ***d***, map showing the extent of the calving event between 1979 and 1986. Grey lines denote all earlier (1947-1978) observed ice frontal positions[5].

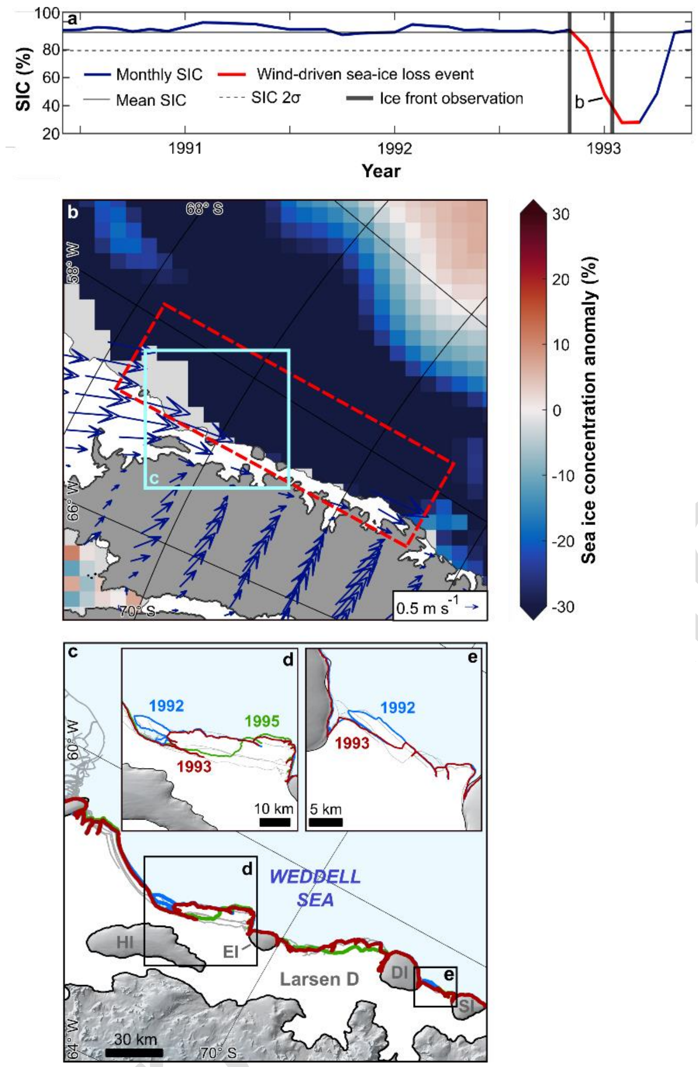

Extended Data Figure 10 | Larsen D coastal sea-ice variability. ***a***, Timeseries showing monthly SIC between 1990 and 1993 when a calving event of uncertain timing occurred (cf. Figure 2). Values represent the average of all cells contained in the red dashed box shown in *b*. Red lines denote times in which highly anomalous (>2σ), wind-driven coastal sea-ice losses would have rapidly de-buttressed Larsen D's ice front, prompted enhanced gravitational ice-shelf flow due to increased (oceanward-down) sea-surface slopes and likely initiated calving. In ***c*** and ***d***, the position of the ice front as observed on 24th January 1995 is also shown, revealing further retreat of the coastline after January 1993 in response to the observed coastal sea-ice loss shown in *a* and *b* and/or the related calving event between December 1992 and January 1993 (*d*). No other satellite imagery exists between these times. *HI* denotes Hearst Island; *EI*, Ewing Island; *DI*, Dolleman Island; *SI*, Steele Island.